# Improved tropical modes of variability in the NCEP Climate Forecast System (version 2) via a stochastic multicloud model

B B Goswami*

*Department of Mathematics and Statistics, University of Victoria, BC, Canada.*

B Khouider

*Department of Mathematics and Statistics, University of Victoria, BC, Canada.*

R Phani

*Indian Institute of Tropical Meteorology, Pune, India*

P Mukhopadhyay

*Indian Institute of Tropical Meteorology, Pune, India*

A J Majda

*Department of Mathematics and Center for Atmosphere and Ocean Sciences, Courant Institute for Mathematical Sciences, New York University, New York, USA and Center for Prototype Climate Models, New York University-Abu Dhabi, Abu Dhabi, United Arab Emirates*

**Corresponding author address:* B B Goswami, Department of Mathematics and Statistics, University of Victoria, BC, Canada.

E-mail: bgoswami@uvic.ca

ABSTRACT

A new stochastic multi-cloud model (SMCM) convective parametrization, which mimics the interactions at sub-grid scales of multiple cloud types, is incorporated into the National Centers for Environmental Prediction (NCEP) Climate Forecast System version 2 (CFSv2) model (referred to as CFSsmcm hereafter) in lieu of the pre-existing simplified Arakawa-Schubert (SAS) cumulus scheme. A detailed analysis of the tropical intra-seasonal variability (TISV) and convectively coupled equatorial waves (CCEW), in comparison with the original (control) model and with observations, is presented here. The last 10-years of a 15-year long climate simulation are analyzed. Significant improvements are seen in the simulation of the Madden-Julian oscillation (MJO) and most of the CCEWs as well as the Indian summer monsoon (ISM) intra-seasonal oscillation (MISO). These improvements appear in the form of improved mechanisms and physical structure of these waves. This can be regarded as a validation of the central idea behind the SMCM according to which organized tropical convection is based on three cloud types namely, the congestus, deep and stratiform cloud decks that interacts with each other and form a building block for multiscale convective systems. An adequate account for the dynamical interactions of this cloud hierarchy thus constitutes an important requirement for cumulus parameterizations to succeed in representing atmospheric tropical variability. SAS fails to fulfill this requirement evident in the unrealistic mechanisms and structures of the major intra-seasonal modes simulated by CFSv2 as documented here.

## 1. Introduction

The tropical atmosphere harbors a spectrum of dynamical modes that interact with each other and with the climate systems, on multiple spatial and temporal (Moncrieff and Klinker 1997; Kiladis et al. 2009; Lau and Waliser 2011). It is still debatable whether these different modes are part of a monster tropical convection belt or are they separate components (Toma and Webster 2010a,b; Serra et al. 2014). The Madden-Julian oscillation (MJO) (Zhang 2005, 2013) and monsoon intra-seasonal oscillations (MISO) (Goswami 2012) dominate the tropical variability on intra-seasonal time-scales and convectively coupled waves (CCEW) and tropical depressions of all sorts are seen on synoptic scales (Kiladis et al. 2009). While CCEWs are thought to be the moist analogs of equatorially trapped waves–linear modes of equatorial dynamics (Matsuno 1966; Takayabu 1994; Wheeler and Kiladis 1999), there is no dry dynamical equivalent mode for the MJO. The atmospheric science community is still debating whether the MJO is a moisture-coupled planetary scale mode or some sort of a multi-scale convective envelope owing its existence to upscale energy transfer from synoptic and mesoscale systems (Majda and Stechmann 2009a; Wang and Liu 2011; Sobel and Maloney 2012; Thual and Majda 2015; Stachnik et al. 2015). Nonetheless, there is a consensus in the climate modeling community that a climate model's ability to simulate the weather and climate realistically depends largely on its ability to simulate these intra-seasonal and synoptic scale modes (Lin et al. 2006; Hung et al. 2013; Jiang et al. 2015). This study aims to gauge, in this regard, the U. S. A. National Centers for Environmental Predictions Climate Forecasting System, version 2 (CFSv2), in which the stochastic multicloud model (SMCM) convective parametrization of (Khouider et al. 2010, hereafter KBM10) is implemented (Deng et al. 2015), in comparison to the original CFSv2 model. In the sequel, the acronym CFSv2 is used to designate the original (control) model while the modified model, using the SMCM parameterization, is termed CFSsmcm.

Despite the significant progress of the last decade or so (Moncrieff et al. 2012, and references therein), present day global climate models (GCM) still show limited ability in simulating the MJO (Slingo et al. 1996; Lin et al. 2006; Kim et al. 2009; Hung et al. 2013; Jiang et al. 2015), MISO (Waliser et al. 2003; Lin et al. 2008b; Sabeerali et al. 2013; Sperber et al. 2013) and CCEWs (Lin et al. 2008a; Straub et al. 2010; Hung et al. 2013; Guo et al. 2015). The inefficiency of the present day climate models to simulate these tropical intraseasonal variability (TISV) modes stems from our limited understanding of tropical dynamics. Recent studies emphasize the importance of representing processes that are thought to be important for TSIV dynamics including moisture pre-conditioning, atmosphere ocean coupling, cloud radiative feedback, convective momentum transport, stratiform heating, and boundary layer dynamics (Lin et al. 2006; Straub et al. 2010; Jiang et al. 2015; Wang et al. 2016a). Nonetheless, there is a consensus in the climate modeling community that the fidelity in proper simulation of the MJO is a pinnacle metric to asses the fidelity of a GCM (Waliser et al. 2009). Straub et al. (2010) found that 75% of the Coupled Model Intercomparison Project (CMIP) phase 3 models fail to realistically simulate the convectively coupled Kelvin waves. Although, the MJO and the CCEWs have a lot in common, improvement in one does not necessarily translate into improvement in the other despite the undeniable evidence that CCEWs, the MJO and mesoscale convective systems are embedded in and interact with each other across multiple temporal and spatial scales (Nakazawa 1988; Moncrieff and Klinker 1997; Gottschalck et al. 2013; Dias et al. 2013). Moreover, both the MJO and the MISO are believed to have an impact on the global weather and climate (Krishnamurthy and Kinter 2003; Zhang 2005, 2013; Lau and Waliser 2011). From clustering synoptic systems (Goswami et al. 2003) to influencing ENSO development (Kirtman and Shukla 2000), TISV modes have profound effects on the tropical variability, the impact being felt much beyond their own spatial and temporal scales. Therefore a model which simulates these TISV modes, viz., MJO, CCEW and MISO, realistically, is expected to simulate the mean state and many other aspects of the global climate with fidelity (Jiang et al. 2015; Kim et al. 2009; Waliser et al. 2009).

The inability of the present day climate models to accurately simulate th prominent TISV modes, is often attributed to their inability to simulate the mean climate state and vice versa (Slingo et al. 1996; Sperber et al. 1997; Gadgil and Sajani 1998; Waliser et al. 2003; Sperber 2004; Lin et al. 2006; Zhang et al. 2006). In this chicken-and-egg dilemma, the synoptic variability has got comparatively less attention. Recently, using 36 coupled models (including 32 CMIP phase 5 models), Goswami and Goswami (2016) argued that the lack of simulated synoptic variability to be partially, at least, responsible for the precipitation dry bias in rain abundant regions of the tropics. The deterministic nature of the convective parameterization (CP) schemes, used in those models, are to be blamed, to some extent, for this as they fail to represent the stochastic nature of convection to trigger organization across multiple scales (Arakawa 2004; Frenkel et al. 2012; Peters et al. 2013). This limitation of the deterministic CP schemes got further exposed when stochastic (Buizza et al. 1999; Lin and Neelin 2000, 2002, 2003; Palmer 2001; Majda and Khouider 2002; Khouider et al. 2003; Plant and Craig 2008; Teixeira and Reynolds 2008; KBM10) and cloud resolving (Grabowski and Smolarkiewicz 1999; Grabowski 2001; Khairoutdinov and Randall 2001; Randall et al. 2003; Satoh et al. 2008; Fudeyasu et al. 2008; Benedict and Randall 2009; Liu et al. 2009) approaches have showed promise. While superparameterized and global cloud resolving models continue to evolve (Goswami et al. 2015; Yashiro et al. 2016; Fukutomi et al. 2016; Kooperman et al. 2016), they remain computationally expensive and impractical. Stochastic approaches are getting more and more consideration (Deng et al. 2015, 2016; Ajayamohan et al. 2016; Davini et al. 2016; Goswami et al. 2016; Dorrestijn et al. 2016; Wang et al. 2016b; Gottwald et al. 2016;

Bengtsson and Kòrnich 2016; Berner et al. 2016; Peters et al. 2017), as a computationally cheap alternative. In this paper, we use the first time the stochastic multicloud model (SMCM) of KBM10 as a cumulus parameterization in a comprehensive GCM.

Previous studies involving the SMCM (KBM10; Khouider et al. 2011; Ajayamohan et al. 2013, 2014, 2016; Deng et al. 2015, 2016) have shown considerable skill in simulating TISV. Using the deterministic multicloud model (DMCM) of Khouider and Majda (2006), hereafter KM06, (see also Khouider and Majda 2008b) as a cumulus parameterization in the National Center for Atmospheric Research (NCAR)'s High-Order Methods Modeling Environment (HOMME), at course GCM resolution, Khouider et al. (2011) demonstrated that the DMCM could simulate many observed features of TISV modes, such as the MJO and CCEWs. Ajayamohan et al. (2013) showed that when a warm pool like background is imposed, the same model exhibits realistic initiation and dynamics of the MJO via circumnavigating Kelvin waves. Deng et al. (2015, 2016) showed that when the SMCM is incorporated into HOMME, in an aqua-planet setup, it produces MJOs with dynamical features such as the front-to-rear vertical tilt and the quadruple vortex structure (Kiladis et al. 2005), and realistic intermittent variability. Ajayamohan et al. (2014, 2016) showed that the simulation of MISOs can be improved by incorporating the SMCM or its deterministic version in the NCAR-HOMME aqua-planet model. However, all of the above results are based on idealized-aquaplanet simulations. Therefore, implementing the SMCM in a fully coupled climate model is an obvious way forward. We took up the NCEP CFSv2 model, promoted by the National Monsoon Mission of the Ministry of Earth Sciences, India, and implemented SMCM in it. Namely, we have replaced the conventional convective parameterization used by CFSv2, which is the Simplified Arakawa-Schubert (SAS) (Pan and Wu 1995; Pattanaik et al. 2013), by the SMCM model.The details of this implementation including the parameter tuning can be found in Goswami et al. (2016), hereafter GKPMM16, and Goswami et al. (2017), hereafter GKPMM17.

The paper is organized as follows. A brief description of the SMCM model formulation is presented in Section 2. Section 3 describes the results, particularly emphasizing the dynamical and physical features of TISV modes, namely, the MJO, CCEW and MISO, as simulated by CFSsmcm in comparison to the control CFSv2 model and observations. Finally, some concluding remarks are given in Section 4.

## 2. Model Equations, Data and Methodology

At this experimental stage of the SMCM parameterization approach, the convective heating profile is based on three prescribed basis functions, which are designed to mimic the three dominating cloud types of tropical convection, namely, congestus, deep and stratiform (Johnson et al. 1999; Mapes et al. 2006). The SMCM divides each GCM grid box into a $40 \times 40$ microscopic lattice. Each lattice site is either occupied by congestus, deep or stratiform cloud decks, or it is a clear sky site. Transitions from a lattice site with one type of cloud to another type occur according to a stochastic-Markov chain process whose transition probabilities depend on the large-scale state through a few convection predictors. New to the CFS implementation (GKPMM16; GKPMM17), the large scale predictors include the convective available potential energy (CAPE), convective inhibition (CIN), middle tropospheric (700 hPa) dryness/moistness (MTD) and vertical velocity at the top of the boundary layer (W). Each microscopic lattice within a large-scale grid box sees the same large scale conditions. However, their evolution in time differ as the transition rules also depend on the previous state of a microscopic lattice, which provides time memory for the cumulus parameterization. The heating rates associated with the three cloud types are parameterized through closure formulas, depending on mid-level moisture and CAPE, that are proportional to the cloud area fractions obtained through the evolving stochastic lattice model. The three prescribed basis functions of the SMCM are amplified by the respective parameterized heating rates and the amplified profiles add up to yield the total parameterized heating. The moisture and temperature tendencies are calculated from this parameterized total heating and then given back to the host model, which is CFSv2.

Specifically, the total convective heating is expressed as (Khouider et al. 2011):

$$Q_{tot}(z) = H_d \phi_d(z) + H_c \phi_c(z) + H_s \phi_s(z).$$

Here, $H_c$, $H_d$ and $H_s$ are the parameterized heating rates associated with the three cloud types, congestus, deep, and stratiform, respectively, while $\phi_d, \phi_d, \phi_s$ are the corresponding heating profile basis functions. Further we have

$$H_d = \sigma_d Q_d, H_c = \sigma_c Q_c, H_s = \sigma_s Q_s$$

with $Q_d, Q_c, Q_s$ are the parameterized heating potentials depending deterministically on CAPE and midlevel moisture and $\sigma_d, \sigma_c, \sigma_s$ are the stochastic area fractions (lattice coverage) occupied by the respective cloud types. These cloud area fractions, along with a fourth state, of sky condition with no clouds, describe a Markov jump stochastic process in the form of a multi-dimensional birth-death system whose transition probabilities depend explicitly on some key large scale predictors motivated by observations and physical intuition (KBM10; Frenkel et al. 2012; De La Chevrotière et al. 2015; Deng et al. 2016). The temperature and moisture convective tendencies are set according to $Q_{tot}$. While, as already mentioned, further details about the implementation of the SMCM convective parametrization in CFSv2 can be found in GKPMM16 and GKPMM17, we note here that except for replacing the SAS cumulus scheme with SMCM, the rest of CFSv2 configuration is unchanged. For instance, CFSsmcm still uses the same shallow cumulus scheme as CFSv2 but the parameterized cloud feedback is ignored. The latter may be included in future versions of CFSsmcm by taking advantage of the stochastic cloud area fractions. Details on the reference model CFSv2 are available in Saha et al. (2014).

We have analyzed the last 10 years output from a 15 year CFSsmcm climate simulation in comparison with a simulation of the same length and same initial conditions, done with the original model, CFSv2, using the SAS convection scheme, as a control run. As an observational benchmark, we used outgoing long-wave radiation (OLR) from NOAA (2.5°x 2.5°; daily) (Liebmann and Smith 1996) and the thermo-dynamical and dynamical parameters from NCEP reanalysis (2.5°x 2.5°; daily) (Kalnay et al. 1996) to evaluate the model simulated climate, using either SMCM or SAS.

For both CFSsmcm and CFSv2 simulations, we used a horizontal resolution of T126, 64 vertical levels, and a time step of 10 minutes. We have extensively used the wavenumber-frequency filtering technique introduced and used by Kiladis et al. (2005, 2009) to isolate the different modes of tropical ISV and the CCEW's.

## 3. Results

In GKPMM16, the CFSsmcm simulation is found to have a reasonably good mean state at least as good as the control CFSv2 model, if not better in some aspects, especially in places where CFSv2 is known to have significant biases. Given that CFSv2 is one of the better of the state-of-the-art climate models, this is a satisfactory result. In this section, the tropical intra-seasonal variability in the CFSsmcm simulation is documented. One standard metric to assess a model-simulated ISV is to plot the Takayabu-Wheeler-Kiladis (TWK for short) spectra (Takayabu 1994; Wheeler and Kiladis 1999). Figure 1 shows the TWK-spectra plotted for the model-simulated OLR for both CFSv2 and CFSsmcm and observations (NOAA OLR, Liebmann and Smith (1996)).

The observed modes have a wealth of literature available for their documentation (Takayabu 1994; Wheeler and Kiladis 1999; Kiladis et al. 2009, and references therein). However, for the sake of completeness, it is worthwhile to list the prominent modes, corresponding to the most significant peaks in Figure 1a. In the symmetric part of the spectrum, we have the eastward moving Madden-Julien oscillation (MJO) corresponding to the peak at wavenumbers 1 to 3 and time periods between 30 to 60 days, westward moving $n = 1$ equatorial Rossby (ER) wave peak at wavenumbers $-3$ to $-4$ and time periods $\sim$ 30 days, Kelvin waves with an elongated peak spanning wavenumbers 2 to 7 and time periods 4 to 10 days, and $n = 1$ westward inertia gravity waves (WIG) roughly around wavenumbers $= -1$ to $-15$ and a time period of 3 days. The antisymmetric part shows one dominant corresponding to westward mixed Rossby-gravity (MRG) waves, between wavenumbers 0 and $-6$ and time periods of 3 to 6 days, and eastward inertia gravity waves (EIG) for wavenumbers 0 to 8 and time periods between 2 and 5 days. The remaining power blobs at negative wavenumbers sandwiched between the WIG and ER waves are believed to correspond to tropical depressions of all sorts including monsoon low pressure systems (Wheeler and Kiladis 1999).

The TISV modes are not prominent in the CFSv2 simulation as indicated by the lack of color contrast in the plots, Fig 1b and 1e. Except for the ER waves, CFSv2 underestimates the power for all the other prominent modes. Moreover, CFSv2 MJO peak has longer time-period than observations (Figure 1b). Significant improvement is evident in the CFSsmcm simulated TWK-spectra (Figure 1e and 1f), including the MJO and especially the higher frequency CCEWs, mentioned above. The MJO period and strength has substantially improved. Also, the Kelvin wave $n = 1$ WIG power have clearly improved in the CFSsmcm. There is a discernible peak corresponding to MRG waves in the CFSsmcm run while it is inexistent in CFSv2. Nonetheless, CFSsmcm simulates a weaker power for most of these modes, compared to observations, and thus there is still room for improvement.

While they obey a rough self similarity feature in vertical structure (Mapes et al. 2006; Kiladis et al. 2009; Khouider et al. 2011), the MJO and the other convectively coupled waves have different propagation properties and different structural details and physical features. The MJO has been one of the most highly studied climate phenomena (Zhang 2005; Wang et al. 2016a, and references therein). A review of the CCEWs can be found in Kiladis et al. (2009). The state of the art models show limited ability in simulating these essential features of the tropical ISV (Lin et al. 2006, 2008b,a; Straub et al. 2010; Hung et al. 2013; Guo et al. 2015; Wang et al. 2016b). Guo et al. (2015) argues that, there is a good chance that a model which simulates the CCEWs realistically would simulate a "good" MJO as well. Therefore, for an in-depth analysis of TISV in CFSsmcm simulations, we isolate the MJO and the different CCEWs applying space-time filtering (Kiladis et al. 2009) and examine the different features. We repeat the same exercise for observations and the control-CFSv2 simulations, for a proper assessment of the improvements.

*a. MJO*

We applied space-time filtering on different meteorological fields and we retained the averaged signal corresponding to wavenumber 1-9 and time-period 30-96 days following Kiladis et al. (2005). We isolated the MJO filtered anomalies for OLR and zonal and meridional wind fields for both the CFSsmcm and the control-CFSv2 simulations and observations (NOAA OLR and NCEP winds, Kalnay et al. (1996)). In Figure 2, the daily variance, for the full year, of the MJO filtered OLR anomalies are shown. In observations (Figure 2b), the maximum variance is seen over the warm waters of the Indian Ocean and western Pacific Ocean, with the peak located over the equatorial Bay of Bengal (BoB). In the western Pacific Ocean, the amplitude is asymmetric about the equator, tilting southward. This is possibly due to the interaction of the MJO with the warm waters of the Indonesian throughflow (Zhou and Murtugudde 2010; Zhang 2013). There is an isolated peak off the gulf of California. In the CFSsmcm simulation (Figure 2a), the variance over the Indian Ocean is reasonably well simulated with the peak slightly shifted south-westward.

Over the western Pacific, the pattern appears patchy with an underestimation towards the southern branch but it remains qualitatively similar to the observations. The peak off the gulf of California is captured well, however one more isolated peak is visible over the south-east Atlantic. In the CFSv2 simulation (Figure 2c), the MJO variance splits into two streaks, distributed north and south of the equator (Figure 2b). Moreover the variance is marginally stronger over the west Pacific than over the Indian Ocean, unlike the observations and the CFSsmcm run. Similarity while a variance pattern is evident, a remnant of the double ITCZ problem is also seen. Overall, CFSsmcm simulated MJO daily variance has greatly improved qualitatively compared to the CFSv2-control simulation.

Figure 3 shows snapshots of an MJO phase composite in terms of the MJO filtered OLR, for different lead times. In order to construct the composite, the peak MJO dates are identified based on an MJO index, corresponding to the MJO filtered anomalies taken at a location of corresponding high variance.We have checked that, the results are resilient to changes in location of this index. The left column of Figure 3, shows the propagation of the MJO filtered OLR anomalies from observations. At 15 days lag, a blob of convection occurs over the west equatorial Indian Ocean (around 60°E). The blob makes a smooth migration eastward and reaches 180°E at a lead time of 25 days. Thus, the convection describes 120 degrees of longitude in 40 days, which corresponds to a phase speed of approximately 5 m $s^{-1}$. During the decay process of the blob, it spreads out and separates onto two blobs south and north of the equator (Lead 25 days).

In the middle column of Figure 3, the phase composite of CFSsmcm simulated MJO filtered OLR anomalies are shown. The overall features of the propagation of convection are reasonably captured. However there are a few striking discrepancies. The first to catch the eye are a smaller spatial extent of the blob and a slower phase speed. Moreover, the active convection over the central Pacific in lag 5 days seems unrealistic but it is very weak. A closer look at this active convection over the central Pacific reveals a wavy pattern indicated by deepening and fading blue shading alternately. This possibly indicates a contamination of the MJO signal by some other modes of variability inherent to CFSsmcm. In comparison, for the CFSv2 MJO filtered OLR anomalies (the third column on the right of Figure 3), the detailed features are hardly resembling the observations. The amplitude and organization of convection are very weak, making it extremely difficult to comment on the phase speed or any other physical property.

The propagation features of the MJO are arguably better characterized by the Hovmöller plots of the MJO composite averaged over the latitude band between 10°S to 10°N, shown in Figure 4. The top three panels, Figure 4a, b and c, show the composites of the MJO filtered anomalies and the bottom three panels, Figure 4d, e and f, show the composite of the corresponding raw (unfiltered) data anomalies for CFSsmcm, NOAA OLR, and the control-CFSv2 simulation, respectively. Consistent with Figure 3 (left column), a smooth propagation is exhibited by the observed OLR data. A feature, which was not evident in Figure 3 and appears clearly in Figure 4b, is the different phase speeds of the MJO, over the Indian Ocean and Pacific Ocean basins. The MJO phase speed is faster over the West Pacific compared to that over the Indian Ocean. In the CFSsmcm simulation (Figure 4a and 4d) the phase speed of the MJO appears slower than observed over the Indian Ocean and the organization is weaker over the West Pacific. Focusing on the MJO filtered anomaly composite Hovmöller plot (Figure 4a), the organization almost seems broken past the maritime continent and reappears in the central Pacific with a hint of eastward movement from there indicating a wavenumber 2 structure. However, when we observe closely the unfiltered composite in Figure 4d, the CFScmcm simulation appears to capture the two different phase speeds on the two sides of the maritime continent, especially for the active phase of convection (blue shading). In the CFSv2 simulations (Figure 4c and f), however, both the organization and amplitude are poorly simulated, consistent with Figure 3 (right column).

Figure 5 shows the circulation features at 850 hPa, top three panels (a, b and c), and at 200 hPa, bottom three panels (d, e and f), of the MJO filtered anomalies for the observations and the two model simulations, as indicated. The observed circulation pattern at 850 hPa (Figure 5b) shows a pair of Rossby gyres north (counter-clockwise) and south (clockwise) and slightly west of the convection peak location with a broad fetch of easterlies over the equatorial Pacific. Two other gyres of opposite signs are also visible east of the convection center but their centers are located far away from the equator–outside the displayed domain. This structure constitutes the famous quadruple structure of the MJO reported in many observational and theoretical studies of the MJO (Rui and Wang 1990; Hendon and Salby 1994; Majda and Biello 2003; Kiladis et al. 2005; Zhang 2005; Majda and Stechmann 2009b). At 200 hPa (Figure 5e), subtropical quadruple rotational circulation enveloping the convective center and winds diverging out of the convection center are seen. The observed circulation patterns at 850hPa and 200hPa indicate a dominantly baroclinic (reversal of wind direction with height) vertical structure for the MJO filtered anomalous winds.

The CFSsmcm simulation (Figure 5a and d) indeed appears to capture this baroclinicity to a good extend. However, the circulation patterns themselves, both at 850hPa (Figure 5a) and at 200hPa (Figure 5d), are not as well organized as in observations, which is consistent with the aforementioned wavenumber 2 type structure of the CFSsmcm simulated MJO. Nevertheless, CFSsmcm captures the major features considerably well: at 850hPa (200hPa), the Rossby gyres (anti-cyclonic circulations) meridionally placed at the two wings of the convection maxima at around 70°E-80°E, underdeveloped in the southern (northern) hemisphere, with westerlies (easterlies) over the Indian Ocean basin and easterlies (westerlies) over the Pacific basin. For the CFSv2 simulations (Figure 5c and f), the circulation patterns look too disorganized to make any conclusive remark.

Figure 6 shows the composite of OLR time series (top panels) and vertical structure of the MJO filtered anomalies, averaged over 5°S-5°N, for CFSsmcm (left column), observations (middle column) and CFSv2 (right column). For a better visualization, each column is topped with its respective OLR variations to locate the convection maximum. It is not hard to see that CFSsmcm simulates the convection activity significantly more realistically than CFSv2. The observed features around the convection maximum (OLR minimum in Figure 6b), like the quadruple structure of horizontal wind in the zonal cross-section (Figure 6e), convergence (divergence) at the lower (upper) troposphere collocated with the OLR minimum (Figure 6h), leading (following) negative (positive) humidity anomalies lead by a lower level moistening (Figure 6k), the collocated positive temperature anomalies (Figure 6n), the collocated updraft with surrounding subsidence (Figure 6q) and the collocated positive anomalous diabatic heating with an extension ahead of the convection maximum in the lower levels (Figure 6t), are reasonably well captured in the CFSsmcm simulation.

The westward tilt (Zhang 2005; Kiladis et al. 2005) prominent in the zonal wind (Figure 6d), convergence (Figure 6g), relative humidity (Figure 6j) and temperature anomalies (Figure 6m), is also captured to a good extent by CFSsmcm. However, the CFSsmcm fields are somewhat noisy and have weaker amplitudes. CFSv2 shows limited skill in capturing these features lacking severely in simulating the adequate organization and amplitude. Noteworthy, in the CFSv2 simulation, the anomalies corresponding to the suppressed phase of convection (OLR maximum) looks more prominent than the active phase. This is clearly visible on the top panels where CFSv2 exhibits a strong OLR positive peak ahead of the convection center and not much of a minimum OLR peak, contrary to CFSsmcm, which is consistent with the observations, with a caveat that the OLR maximum is ahead of the minimum in the observation but the former lags the latter in CFSsmcm. Nonetheless, this difference is perhaps simply an artifact of the compositing technique.

### *b. CCEW*

In order to verify whether the structure and propagation features of the simulated CCEW modes are well simulated, here we isolate the different individual modes by applying a space-time filtering and examine the different features as done for the MJO. The space-time filters used here are the same as the ones used in Kiladis et al. (2009), except for the $n = 0$ EIG waves for which we used a narrower region, limited by wavenumbers 1 to 3, frequencies 0.166 to 0.55, and equivalent depth curves $H = 12$ m and $H = 50$ m. A broader filter as in Kiladis et al. (2009) makes the EIG signal contaminated with Kelvin waves, as the latter appear stronger in the CFCsmcm simulation. An alternative would be to separate the solution into symmetric and antisymmetric parts but we refrained from doing that here because it is not standard practice.

Figure 7 shows the daily variances corresponding to the different modes of the CCEW spectrum for CFSsmcm simulation (left column), observations (middle column) and CFSv2 simulation (right column). The maximum variance for all the displayed modes are observed to be over the west to central Pacific region. In the CFSsmcm simulations (left column panels) the overall pattern and amplitude of the different variances are well captured however the peak variance is slightly shifted westward for almost all the modes. Variance for the Kelvin, EIG and MRG modes are slightly under-estimated whereas, that of the ER and WIG are slightly over-estimated. CFSv2 (right column panels) severely underestimates the daily variance for all the modes, except ER waves, which are overestimated, on the contrary. CFSsmcm also simulates an overestimated ER daily variance, but the CFSv2 overestimation is larger. The black lines are drawn to highlight the maximum variance region, over which the composite anomalies are averaged to explore the propagation features of the different CCEWs in Figure 8.

The propagation features, shown in Figure 8, are captured reasonably well by CFSsmcm: eastward propagating Kelvin and EIG waves and westward propagating ER, WIG and MRG waves. The phase speeds are simulated marginally slowly (more so for the EIG waves), except for the MRG waves. The westward shift of the maximum variance, observed in CFSsmcm simulations in Figure 7, are now prominently visible. In fact, the slower phase speeds are maybe connected to this westward shift. Overestimation of ER waves is also more evident now. Except for the ER waves, CFSv2 simulated CCEWs have weak amplitudes. The most striking improvements are seen in the simulation of the Kelvin, inertia gravity and MRG waves by CFSsmcm, compared to CFSv2.

The 850 hPa and 200hPa composite circulation patterns corresponding to the peak phase of the different CCEWs are shown in Figures 9 and 10, respectively, superimposed on the corresponding OLR anomalies. The observed circulation features are reasonably well simulated by the CFSsmcm simulation, including equatorial low level westerlies and low level easterlies convergent to the active convection center for the Kelvin wave (Figure 9b), a the train of cyclonic and anticyclonic circulation patterns flanking both sides of the equator and collocated with the active and suppressed centers of convection for the ER wave (Figure 9e), and a train of cyclonic and anticyclonic circulations over the equator binding the convective centers located on the four quadrants of the circulation pattern for the MRG wave (Figure 9n). The simultaneous meridional and zonal convergent streamlines in the Kelvin wave composites in the CFSsmcm and to some extent in the observation are consistent with the structure of Kelvin waves evolving in a meridional jet shear background (Roundy 2008; Ferguson et al. 2010; Han and Khouider 2010). For the ER (Figure 9d) and MRG (Figure 9m) waves, the convection is underdeveloped south of the equator. Also the location of the simulated convective centers corresponding to the ER wave (Figure 9d), in the northern hemisphere, are shifted considerably south of the observed locations (Figure 9e).

In the CFSv2 simulated climate, the pattern of the OLR anomalies are realistically captured, however, they are underestimated, except for the ER waves, which is consistent with Figures 7 and 8. Also except for the ER (Figure 9f) and MRG (Figure 9o), the model misses the major circulation features. The WIG (Figure 9l) waves particularly look very poorly simulated.

At 200hPa, the observed winds (Figure 10, middle column) are reversed relative to 850hPa winds due to baroclinicity, and are relatively stronger than at 850hPa. The improvements in the winds at 200hPa, are consistent with the improvements seen in the 850hPa level, in CFSsmcm simulations. To avoid, redundancy we are keeping away from a detailed description of the features observed in the 200hPa level. Realistic circulations at lower (850hPa) and upper (200hPa) levels indicate better heating profiles associated with these modes. For CFSv2 as well, the circulation patterns at 200hPa level appears consistent with the 850hPa pattern, in terms of baroclinicity. However, like in the 850hPa level, the simulated winds are weaker and the circulation patterns lack organization. Overall, the convection and circulation patterns associated with the different CCEW modes (in their peak phase) are simulated significantly better in CFSsmcm than in CFSv2 climate.

### *c. MISO*

The Indian summer monsoon (ISM) intra-seasonal oscillations (ISO) or MISOs constitute a major component of the tropical climate variability. Like the MJO, the state-of-the-art climate models find it difficult to simulate MISOs as well (Lin et al. 2008b; Sabeerali et al. 2013). There is still a debate on whether the boreal summer MISO mode is distinct from the eastward propagating MJO mode apart from the fact that the former is prominent in the boreal summer while the latter is dominant in winter (Lau and Chan 1986; Kikuchi et al. 2012). Nonetheless, the MJO has an equatorially trapped spatial structure, whereas the MISO shows an off-equatorial structure with strong convective activity over the south Asian region. In fact, the challenges of simulating MJO and MISO are similar. It is believed that they are both conditioned by a proper representation of organized convection as in essence they are both a byproduct of the latter. In Section 3a, we have seen that CFSsmcm has significantly improved the simulation of the MJO compared to the host model. Moreover, GKPMM16 has shown that the distribution of rainfall has also improved in the CFSsmcm simulation, especially over India.

In order to investigate the ISM intra-seasonal variability, we plot the north-south version of the TWK-spectra and the conventional east-west TWK-spectra (Figure 11), but for the boreal summer season only. Noteworthy, for the north-south TWK-spectra (Figure 11a, c and e), wavenumber 1 corresponds to 50 degrees of latitude (from 20°S to 30°N). In observations (Figure 11a), we notice a northward propagating mode with time-period of about 45 days and centered at wavenumber 1. For comparable time period and wavenumber, a southward component is also noted, but with less power.

Comparing the model simulations (CFSsmcm in Figure 11c and CFSv2 in Figure 11e) with observations, we can see that both models capture the northward and southward propagating components but with a longer time period of about 60 days, though the CFSsmcm signal seems to extend to higher frequencies. Also, the power in the MISO modes is slightly underestimated, more so in CFSsmcm simulations. In the east-west TWK spectra (Figure 11b), the dominant power, seen around wavenumbers 1 to 2 and time period 45-days, correspond to the eastward moving ISOs or MJOs. The power in the 45-day time period in both the north-south and east-west spectra is consistent with the fact that MISOs predominantly propagate northeastward (Lau and Chan 1986; Goswami 2012). Eastward moving Kelvin waves and westward ER waves are also seen in the spectra (Figure 11b). Power in the 10-20 day range propagating westward indicate 10-20 day high-frequency ISOs (Goswami 2012).

In the two model-simulations, CFSsmcm simulated spectra (Figure 11f) looks more realistic than that of CFSv2 (Figure 11d). CFSv2 simulates unrealistic eastward power at higher wavenumbers. Also it simulates spurious power all along the positive wavenumber axis. The westward ER wave power is overestimated by CFSv2 and it peaks at a much longer period $\sim$ 60 days. Also it simulates a weak power for the Kelvin waves, which is consistent with Figure 1b and the 10-20 day westward ISO power is underestimated.

The eastward power at 60-days in Figure 11f is consistent with the power at the same time-period in Figure 11e. This indicates a possibility of realistically simulating the northeastward movement of the monsoon trough by CFSsmcm. Noteworthy, the lack of eastward power about wavenumber 1 (Figure 11d), in the backdrop of CFSv2 simulating reasonable power corresponding to associated northward propagation, is unrealistic and raises suspicion about the simulated propagation mechanism. CFSv2 fails to simulate the desired power for the westward propagating 10-20 day high frequency monsoon ISOs and it is slightly overestimated in the CFSsmcm simulations. In the remainder of this section, we analyze the 45-day MISO or simply the MISO dynamical structure and physical properties as simulated by the two models. In order to isolate the MISO anomalies, we apply space-time filtering as we have done in Sections 3a and 3b. However, we apply the filter only for the boreal summer data. Based in the spectra shown in Figure 11 we use the filter with the time-period range 20-100 days and wavenumber range 0 to 4. The anomalies isolated for MISO are plotted in Figures 12, 13 and 14.

The boreal summer MISO daily OLR variance is plotted in Figure 12a, b and c for CFSsmcm, observation (NOAA OLR data), and CFSv2, respectively. In observations (Figure 12b), the maximum variance is located in the northern Indian Ocean and West Pacific, with the peak at the head of the Bay of Bengal and the high variance contours displaying a northwest-southeast orientation. Noteworthy, all the high variance zones are over the oceanic regions in both models and observations. The titled orientation of the variance pattern is missing in both model-simulations (CFSsmcm in Figure 12a and CFSv2 in Figure 12c). CFSsmcm fails to capture the peak in the head of the Bay of Bengal region. It is shifted over the Arabian Sea, instead. In fact, the whole CFSsmcm MISO variance, over the west Pacific, is shifted eastward and it is slightly overestimated. This eastward variance shifting is symptomatic and it is utterly consistent with that of the MJO and CCEWs in Figures 2 and 7. It won't be surprising if the ocean model is the culprit and a thorough investigation of this matter is warranted.

CFSv2 simulates an overestimated peak at the head of the Bay of Bengal and also highly overestimates the variance over the west Pacific. This is consistent with the work of Goswami et al. (2014, 2015) who showed that CFSv2 tends to overestimate the low frequency ISV. As per the variance plots, both models have difficulties in simulating the daily variance of the MISO though the CFSsmcm simulation has noticeable improvements. The most significant improvements include an extended power over continental India as in the observations and a significant reduction of the faulty power over the Western Pacific and the Bay of Bengal.

The northward propagation feature of MISO is examined by plotting meridional Hovmöller diagrams, averaged over 65°E-95°E, of a composite of the MISO filtered OLR anomalies. The composite is constructed based on an index located over the Bay of Bengal. In observations (Figure 12e), the MISOs start migrating approximately from 10°S and go up to 25°N with a phase speed of about 1.5°Lat per day. CFSsmcm (Figure 12d) captures this phase speed realistically and the convection starts migrating from about 10°S as in the observations. The amplitude, however, is weaker. CFSv2 simulated MISOs (Figure 12f) also appear to be weaker than the observations but they also have a slower northward propagation and the migration starts right at the equator, unlike in the observations and in CFSsmcm. The convection pattern south of 10°S looks spurious in the CFSv2 simulation.

The composite circulation patterns for the peak MISO phase at 850 hPa superposed on the corresponding OLR anomalies are shown Figure 12g, h and i for CFSsmcm, observations (OLR from NOAA and winds from NCEP) and CFSv2, respectively. In the observations (Figure 12h), a monsoon trough like organization is evident in the OLR anomalies. This is accompanied by a Rossby gyre-type pair of cyclonic circulations at 850 hPa with a fetch of easterlies emanating from the northern Pacific Ocean blowing over India and strong westerlies over the Indian Ocean. These features are similar to what we had observed in the circulation patterns for the MJO peak phase shown in Figure 5b, at least for the Rossby gyres and Equatorial westerlies somewhat lagging the convection core. A third gyre can be seen in north-eastern India.

The CFSsmcm (Figure 12g) simulated OLR anomalies rather appear to have a "blob" like structure instead of a monsoon trough-like orientation in the sense that it is not extended in the north-westward direction. However it captures the cyclonic circulation slightly north of the convection maximum reasonably well but it underestimates the one to the south; it is somewhat shifted to the west allowing the north-westerly winds to penetrate into the Arabian sea. This is perhaps connected with the lack of elongation of the OLR signal. The easterlies over the Pacific are captured reasonably well, but they look wobbly. The third gyre is shifted North East. Again, these biases are somewhat similar to the issues discussed while describing CFSsmcm simulated circulation pattern for the peak MJO phase (Figure 5a).

In the CFSv2 simulation (Figure 12i), the peak of the OLR anomalies are heavily shifted eastward compared to the observations. Moreover the simulated monsoon trough-like OLR anomaly pattern has an overestimated meridionally oriented component extending to 30°S. Nevertheless, the CFSv2 simulated circulation pattern, looks reasonably simulated and somewhat better than CFSsmcm (comparing Figure 12g and i) except for the fact that the Southern tail of the whole pattern is shifted to the west.

The winds over the west Pacific are observed to be dominantly westerlies, at 200hPa. Comparing the observed winds at 850hPa and 200hPa we note, the circulations are neither dominantly baroclinic nor barotropic. This is a feature of the MISO that is different from MJO, which is dominantly baroclinic (Figures 5b and e). This in fact makes the MISOs a dynamically complex component of the tropical climate and a difficult feature for the climate models to simulate. CFSsmcm simulates the 200hPa circulation patters for the peak MISO phase with considerable fidelity. However, the cyclonic circulation north-west of the convection maximum looks unrealistic. Nevertheless, comparing the 200hPa circulation relative to the 850hPa winds in the CFSsmcm simulations, the model seems to capture the baroclinic-barotropic nature of the MISO circulation reasonably well. CFSv2 simulated winds at 200hPa (Figure 12l) shows limited ability in simulating the major observed features. The fact that, CFSv2 simulates a "too much" meridional orientation of the convective band by simulating the 850hPa circulation with considerable success while missing the major circulation features at the 200hPa level suggests the possibility of an unrealistic dynamics in the model.

In Figure 13, the vertical structure of the MISO mode is examined. This figure is similar to Figure 6, but for MISO. The panels in Figure 13 show the height-latitude cross sections of different fields averaged over 70°E-90°E. The top panels show the meridional variation of the corresponding OLR with the minimum indicating the peak convection. In observations, the convection peak is seen at around 7°N (Figure 13h). The impression of the cross-equatorial south-westerly ISM low level jet is seen in Figure 13i, where the zero (meridional) shear line is slightly north (10°N) of the convection maximum. Around the same location, "convergence below and divergence aloft" feature is seen in Figure 13j. Positive moisture anomalies with a significant southward tilt dominate the atmosphere south of 17°N and negative anomalies northward beyond 17°N (Figure 13k). At about 10°N, negative temperature anomalies are seen at the lower troposphere (below 600hPa) and positive anomalies aloft (Figure 13l). Updrafts throughout the atmospheric column are collocated with the convection maximum (Figure 13m). The updraft maximum is led by downdraft northward and followed (from the south) by a region of mild updraft in the middle troposphere and downdraft in the lower and upper troposphere. The diabatic heating shows positive anomalies collocated with the convection peak, the maximum heating being at 400-500hPa (Figure 13n). The positive anomalies are led by negative anomalies northward and followed by mild positive anomalies in the middle troposphere. The observational features noted above are consistent with the shear-vorticity driven northward propagation mechanism of MISOs (Jiang et al. 2004).

CFSsmcm reasonably captures the major features, as noted in the OLR meridional profile, zonal wind, convergence and temperature anomalies (Figures 13a, b, c and e). The only major concerns of the CFSsmcm simulation are the dry moisture bias immediately south of the equator at about 5°S (Figure 13d) and the very narrow and highly overestimated values of updrafts (Figure 13f) and diabatic heating rates (Figure 13g). In the CFSv2 simulation (Figure 13 o-u) all the fields are found to have major biases. The biases in the zonal wind, convergence and moisture fields are particularly grave in the backdrop of the fact that CFSv2 simulates reasonable northward propagating MISOs. The lack of barotropic shear vorticity line and the northward tilt of the moisture anomalies are particularly disturbing. It seems like CFSv2 captures the northward propagation of MISO for the wrong reasons.

There is significant evidence that it is the low level moisture convergence north of the convection maximum that drives the convection northward. Jiang et al. (2004) argued that, a heat source in the presence of an easterly mean flow leads to a cyclonic barotropic vorticity centered slightly to the north, which in turn drives the frictional convergence in the boundary layer, consistent with the finding of De La Chevrotière and Khouider (2017) who coupled the SMCM to an idealized three layer zonally symmetric model monsoon-like simulation. In a recent study, Hazra and Krishnamurthy (2015) argued that moisture anomalies may provide the necessary preconditioning to promote the northward propagation of MISOs, a mechanism analogous to the preconditioning mechanism in the case of MJOs (Jiang et al. 2011; Khouider et al. 2011). Abhik et al. (2013) also argues in favor of preconditioning mechanism for northward propagation of the MISOs. Noteworthy, the SMCM framework is in fact designed to mimic the congestus preconditioning in the tropics (KM06; KBM10). Motivated by these arguments, we have explored the preconditioning mechanism for the northward propagation of the MISOs.

Figure 14 shows the composite phase-wise latitude-height cross-sections (averaged over 70°E-90°E) of diabatic heating superimposed on the moisture anomalies. The observations are shown on the left column. The red contours show the heating associated with the MISO convection, which starts over the equator and propagates poleward till 20°N. The heating shows a top heavy vertical structure with the peak heating observed around 400-500hPa level attaining a maximum value of 2 K day$^{-1}$ in phases Lag 0 and Lag +5. The associated specific humidity field, shown in shading, indicates a bottom heavy profile with positive moisture anomalies leading the heating maximum in the lower troposphere synonymous of moisture preconditioning ahead of the convection (indicated by the heating contours) driving the convection northward. Both the heating and moisture fields exhibit a north-south vertical tilt, leaning backward at the upper troposphere.

The CFSsmcm simulation (in the middle column) captures this tilted structure reasonably well, in both the heating and moisture fields despite a few discrepancies, such as an overestimation of the heating maximum, an earlier peak, and a limited poleward extension. Nevertheless, the moisture preconditioning ahead of the convection maximum is captured well. This preconditioning feature is missing in the CFSv2 simulation (extreme right column). The positive and negative heating contours are in phase with the positive and negative shadings of specific humidity, respectively.

Arguably, the titled vertical structure is backward (and more prominent in the negative heating contours) compared to the observations.

The heating is overestimated in the CFSv2 simulation as in the CFSsmcm simulation, however in CFSv2 the poleward propagation is observed to reach 20°N like the observations. However, the moisture and heating maxima are in phase and CFSv2 seems to lack the main moisture preconditioning mechanism, which raises the same questions as the the MJO. In the absence of the preconditioning mechanism, what is the mechanism responsible for the northward propagation of the MISOs in the CFSv2 simulated climate? Noteworthy, CFSsmcm simulated MISO northward propagation mechanism appears to be consistent with the hypothesis of Jiang et al. (2004) and it is realistic. The realistic simulation of the moisture preconditioning in CFSsmcm climate is undoubtedly related to the prescribed cloud-type trilogy in the SMCM formulation and its ability to simulate the other TISV modes.

## 4. Discussion and Conclusion

A 15 year simulation with NCEP's coupled climate model CFSv2, in which a new stochastic multicloud model (SMCM) cumulus scheme was implemented (GKPMM16; GKPMM17), CFSsmcm for short, was analyzed here against a control simulation of the same length and same initial conditions, in terms of its ability to capture the main modes of tropical variability on synoptic and intra-seasonal scales, including the MJO, CCEWs, and MISO. NOAA OLR (Liebmann and Smith 1996) and NCEP reanalysis fields (Kalnay et al. 1996) are utilized as an observational benchmark. SMCM aims to capture the statistics of the subgrid variability of the three could types, cumulus congestus, deep and stratiform (KBM10, Frenkel et al. 2012; Peters et al. 2013; De La Chevrotière et al. 2015), that are observed to characterize multi scale tropical convective systems, including the MJO and CCEWs (e.g.,Johnson et al. 1999; Mapes et al. 2006; KM06). As such CFSsmcm captures most of the spectrum of tropical intra-seasonal variability with great fidelity including many of their physical and dynamical features while the control model performed very poorly overall. Though there is still room for further improvements, the performance of CFSsmcm is somehow expected based on the previous successes of the SMCM in the context of an aquaplanet atmospheric GCM (Khouider et al. 2011; Ajayamohan et al. 2013, 2014, 2016; Deng et al. 2015, 2016) and the fact that the SMCM is rooted from the thoroughly documented theoretical framework of the multicloud model for convectively coupled waves (KM06; Khouider and Majda 2007, 2008a,b; Han and Khouider 2010).

The first striking improvement is seen in terms of the Takayabu-Wheeler-Kiladis diagram (Takayabu 1994; Wheeler and Kiladis 1999) in Figure 1. While the control run, CFSv2, has a limited skill in this regard, CFSsmcm shows significant improvements essentially by adding power to the Kelvin, MRG, WIG, and EIG waves, most of which are weaker or inexistent in the control run. The MJO frequency is also improved. Nonetheless, the superiority of the CFSsmcm simulation is more appreciated when digging deeper and looking at the physical and dynamical features of these waves.

The physics and dynamics of the MJO are presented in Section 3a. In terms of the geographical distribution of MJO variance, while both simulations exhibit a fair amount of power over the bulk area of the tropical warm pool, they both show some limitations when compared to NOAA OLR. While CFSsmcm suffers from a severe westward shift of the variance maximum, the control run exhibits an unrealistic double peak, each of which are located on either side of the equator somewhat reminiscent of the double ITCZ problem. One of the most visible striking outperformance of CFSsmcm comes in terms of the propagation of MJO filtered OLR composites in Fig 3. While CFSsmcm shows a clear propagating blob of low OLR, with the right phase speed and geographical location and amplitude as in the observation, CFSv2 fails miserably in this regard. The same consistent behavior is seen in the Hovmöller plots in Figure 4. Also the famous quadruple vortex structure and associated baroclinicity of the MJO (Rui and Wang 1990; Hendon and Salby 1994; Majda and Biello 2003; Kiladis et al. 2005; Zhang 2005; Majda and Stechmann 2009b) are reasonably captured by CFSsmcm while the horizontal flow structure of CFSv2 is completely disorganized.

The vertical structure in Figure 6 raises the question whether the MJO-power spectrum peak exhibited by the CFSv2 simulation in Figure 1 has anything in common with the MJO as a physical mode of tropical variability. CFSv2 lacks the most fundamental dynamical and morphological features such as the absence of a pronounced OLR minimum or any of the fundamental characteristics of the dynamical fields while CFSsmcm compares relatively well to the observations in all aspects, including the backward tilt in moisture, horizontal wind, and temperature (Kiladis et al. 2005, for e.g.). In particular, the persistence of low-level moistening and congestus (low-level) heating, during the suppressed phase of the MJO for about two to three weeks (60-80 deg divided by 5 m $s^{-1}$) prior to the MJO active convection, which is observed in both the CFSsmcm simulation and the reanalysis MJO plots but absent in the control CFSv2 MJO, as illustrated in Figure 6, is consistent with the idea that congestus heating serves to moisten the environment prior to deep convection as demonstrated by in situ observation from the CINDY/DYNAMO observation campaign (Johnson and Ciesielski 2013; Bellenger et al. 2015; Chen et al. 2015) and detailed numerical and theoretical studies (Derbyshire et al. 2004; Waite and Khouider 2010; Hohenegger and Stevens 2013; Hirons et al. 2013).

The faithful representation of the MJO's main physical and dynamical features in the CFSsmcm simulation stems from the design principles of the stochastic multicloud model based on the self-similar morphology and dynamics of multiscale tropical convective systems (KM06; KBM10) and is consistent with previous studies using the deterministic and stochastic multicloud model

(Khouider et al. 2011; Ajayamohan et al. 2013, 2014, 2016; Deng et al. 2015, 2016). The superiority of the stochastic simulation, as opposed to global simulations using the deterministic MCM, comes from the fact that the stochastic model is able to simultaneously put variability at a wide range of scales, ranging from meso- to planetary scales in an intermittent fashion (Frenkel et al. 2012, 2013; Deng et al. 2016) although, the main linear instabilities, for the considered parameter regimes, exhibited by the (deterministic) multi-cloud model, occur at synoptic scales (KM06; Khouider and Majda 2008a,b; Han and Khouider 2010; Khouider et al. 2012).

The simulation of Kelvin waves has always been found to be good in the CFSsmcm simulation even during the tuning of the model (Goswami et al. 2017). We presume that these improvements in the CCEWs come by virtue of a better simulation of the convective heating profiles, which take into account the proper dynamical interactions of the three cloud types with the large-scale moisture and other thermodynamical fields. Although currently we do not have a solid evidence to support this claim, the improvements in the associated circulation patterns, shown in Figures 9 and 10, backs this well, consistently with the design principle of the multicloud model (KM06; Khouider and Majda 2008a,b; Han and Khouider 2010; Khouider et al. 2011, 2012).

Except for equatorial Rossby waves, CFSv2 shows very little to no power in terms of the distribution of OLR variance of CCEWs as shown in Figure 7 while CFSsmcm performs relatively well in this regard. However, there are some visible discrepancies when comparing CFSsmcm to the observations, including a westward shift of the maximum variance, particularly for the Kelvin and EIG waves, and differences in amplitude. The westward variance shift is consistent with that of the MJO and it won't be surprising if they have the same common origin. Curiously, these are all eastward moving signals. The propagation characteristics and horizontal structures of these waves are equally well captured by the CFSsmcm simulation according to Figures 8 through 10. It has to be noted at this point that these are T126 simulations and some features of these waves (such as their convective cores) are represented by less than 5 grid points in one horizontal direction.CFSv2 does a good job in representing the structure and propagation of the equatorial Rossby waves consistent with the spectral power plot in Figure 1.

Last but not the least, the capability of CFSsmcm to capture the physical and dynamical features of the Indian MISO is assessed in Section 3c and Figures 11 through 14. First, from Figure 12, the distribution of the MISO-filtered OLR variance is captured relatively well compared to the control run that puts too much power over the western Pacific and the Bay of Bengal. Also the northward propagation over the Indian Ocean and continental India, which appears to be too slow and has a too weak amplitude and starts migrating right at the equator instead of 10°S, in the CFSv2 control run, is considerably corrected in the CFSsmcm run. Moreover, while the vertical structure of this mode is well captured by CFSsmcm, compared to observation as shown in Figure 13, hinting to the shear vorticity–moisture preconditioning mechanism (Jiang et al. 2004; Abhik et al. 2013; Hazra and Krishnamurthy 2015) being at work, the CFSv2 MISO signal has too little in common with this mechanism. Arguably, the northward propagating ISO in CFSv2 obeys completely different physics than what actually occurs in nature and the same can be said about its MJO. Indeed, the fact that CFSsmcm captures the physical and dynamical features of the main tropical modes of variability is not a matter of serendipity but can be rooted to the theoretical foundation and empirical evidence of the SMCM (KBM10; Peters et al. 2013; De La Chevrotière et al. 2015) and its parent deterministic multicloud model (KM06) which is build based on intuition guided by observations (Lin and Johnson 1996; Johnson et al. 1999). The results shown here are yet another demonstration that tropical convective variability is both multiscale and self-similar in nature and most of it can be explained by the complex interactions of the three key cloud types, congestus, deep, and stratiform, with the dynamical and moisture fields, by shaping up the vertical structure of the diabatic heating, on multiple time and spatial scales.

*Acknowledgments.* The research of BK is partially funded by a grant from the Government of India through the National Monsoon Mission (NMM) and a discovery grant from the Canadian Natural and Sciences and Engineering Research Council. BBG is a post doctoral fellow through BK's NMM grant.

## References

Abhik, S., M. Halder, P. Mukhopadhyay, X. Jiang, and B. Goswami, 2013: A possible new mechanism for northward propagation of boreal summer intraseasonal oscillations based on TRMM and MERRA reanalysis. *Clim. Dyn.*, **40 (7-8)**, 1611–1624, doi:10.1007/s00382-012-1425-x.

Ajayamohan, R. S., B. Khouider, and A. J. Majda, 2013: Realistic initiation and dynamics of the Madden-Julian Oscillation in a coarse resolution aquaplanet GCM. *Geophys. Res. Lett.*, **40 (23)**, 6252–6257, doi:10.1002/2013GL058187.

Ajayamohan, R. S., B. Khouider, and A. J. Majda, 2014: Simulation of monsoon intraseasonal oscillations in a coarse-resolution aquaplanet GCM. *Geophys. Res. Lett.*, **41 (15)**, 5662–5669, doi:10.1002/2014GL060662.

Ajayamohan, R. S., B. Khouider, A. J. Majda, and Q. Deng, 2016: Role of stratiform heating on the organization of convection over the monsoon trough. *Clim. Dyn.*, 1–20, doi:10.1007/s00382-016-3033-7.

Arakawa, A., 2004: The cumulus parameterization problem: Past, present, and future. *J. Clim.*, **17 (13)**, 2493–2525, doi:10.1175/1520-0442(2004)017⟨2493:RATCPP⟩2.0.CO;2.

Bellenger, H., K. Yoneyama, M. Katsumata, T. N. andK. Yasunaga, and R. Shirooka, 2015: Observation of moisture tendencies related to shallow convection. *J. Atmos.Sci.*, **72 (2)**, 641–659, doi:10.1175/JAS-D-14-0042.1.

Benedict, J. J., and D. A. Randall, 2009: Structure of the Madden-Julian oscillation in the super-parameterized CAM. *J. Atmos. Sci.*, **66 (11)**, 3277–3296, doi:10.1175/2009JAS3030.1.

Bengtsson, L., and H. Kòrnich, 2016: Impact of a stochastic parametrization of cumulus convection, using cellular automata, in a mesoscale ensemble prediction system. *Q. J. R. Meteorolog. Soc.*, **142 (695)**, 1150–1159, doi:10.1002/qj.2720.

Berner, J., and Coauthors, 2016: Stochastic parameterization: Towards a new view of weather and climate models. *Bull. Am. Meteorol. Soc.*, **0 (0)**, doi:10.1175/BAMS-D-15-00268.1.

Buizza, R., M. Milleer, and T. N. Palmer, 1999: Stochastic representation of model uncertainties in the ECMWF ensemble prediction system. *Q. J. R. Meteorolog. Soc.*, **125 (560)**, 2887–2908, doi:10.1002/qj.49712556006.

Chen, S., and Coauthors, 2015: A study of CINDY/DYNAMO MJO suppressed phase. *J. Atmos.Sci.*, **72 (10)**, 3755–3779, doi:10.1175/JAS-D-13-0348.1.

Davini, P., and Coauthors, 2016: Climate SPHINX: evaluating the impact of resolution and stochastic physics parameterisations in climate simulations. *Geosci. Model Dev. Discuss.*, **2016**, 1–29, doi:10.5194/gmd-2016-115.

De La Chevrotière, M., and B. Khouider, 2017: A zonally symmetric model for the monsoon-Hadley circulation with stochastic convective forcing. *Theor. Comput. Fluid Dyn.*, **31 (1)**, 89–110, doi:10.1007/s00162-016-0407-8.

De La Chevrotière, M., Michèle, B. Khouider, and A. Majda, 2015: Stochasticity of convection in Giga-LES data. *Clim. Dyn.*, **47 (5)**, 1845–1861, doi:10.1007/s00382-015-2936-z.

Deng, Q., B. Khouider, and A. J. Majda, 2015: The MJO in a coarse-resolution GCM with a stochastic multicloud parameterization. *J. Atmos. Sci.*, **72 (1)**, 55–74, doi:10.1175/JAS-D-14-0120.1.

Deng, Q., B. Khouider, A. J. Majda, and R. S. Ajayamohan, 2016: Effect of stratiform heating on the planetary-scale organization of tropical convection. *J. Atmos. Sci.*, **73 (1)**, 371–392, doi:10.1175/JAS-D-15-0178.1.

Derbyshire, S. H., I. Beau, P. Bechtold, J.-Y. Grandpeix, J.-M. Piriou, J.-L. Redelsperger, and P. M. M. Soares, 2004: Sensitivity of moist convection to environmental humidity. *Quart. J. Roy. Met. Soc.*, **130**, 3055–3080, doi:10.1256/qj.03.130.

Dias, J., S. Leroux, S. N. Tulich, and G. N. Kiladis, 2013: How systematic is organized tropical convection within the MJO? *Geophys. Res. Lett.*, **40 (7)**, 1420–1425, doi:10.1002/grl.50308.

Dorrestijn, J., D. T. Crommelin, A. P. Siebesma, H. J. Jonker, and F. Selten, 2016: Stochastic convection parameterization with Markov Chains in an intermediate-complexity GCM. *J. Atmos. Sci.*, **73 (3)**, 1367–1382.

Ferguson, J., B. Khouider, and M. Namazi, 2010: Two-way interactions between between equatorially trapped waves and the barotropic flow. *Chin. Ann. Math. Ser. B*, **30**, 539–568, doi:10.1007/s11401-009-0102-9.

Frenkel, Y., A. J. Majda, and B. Khouider, 2012: Using the stochastic multicloud model to improve tropical convective parameterization: A paradigm example. *J. Atmos. Sci.*, **69 (3)**, 1080–1105, doi:10.1175/JAS-D-11-0148.1.

Frenkel, Y., A. J. Majda, and B. Khouider, 2013: Stochastic and deterministic multicloud parameterizations for tropical convection. *Clim. Dyn.*, **41 (5-6)**, 1527–1551, doi:10.1007/s00382-013-1678-z.

Fudeyasu, H., Y. Wang, M. Satoh, T. Nasuno, H. Miura, and W. Yanase, 2008: Global cloud-system-resolving model NICAM successfully simulated the lifecycles of two real tropical cyclones. *Geophys. Res. Lett.*, **35 (22)**, doi:10.1029/2008GL036003.

Fukutomi, Y., C. Kodama, Y. Yamada, A. T. Noda, and M. Satoh, 2016: Tropical synoptic-scale wave disturbances over the western Pacific simulated by a global cloud-system resolving model. *Theor. Appl. Climatol.*, **124 (3)**, 737–755, doi:10.1007/s00704-015-1456-4.

Gadgil, S., and S. Sajani, 1998: Monsoon precipitation in the AMIP runs. *Clim. Dyn.*, **14 (9)**, 659–689, doi:10.1007/s003820050248.

Goswami, B. B., M. Deshpande, P. Mukhopadhyay, S. K. Saha, S. A. Rao, R. Murthugudde, and B. N. Goswami, 2014: Simulation of monsoon intraseasonal variability in NCEP CFSv2 and its role on systematic bias. *Clim. Dyn.*, **43 (9-10)**, 2725–2745, doi:10.1007/s00382-014-2089-5.

Goswami, B. B., and B. N. Goswami, 2016: A road map for improving dry-bias in simulating the south Asian monsoon precipitation by climate models. *Clim. Dyn.*, **0 (0)**, null, doi:10.1007/s00382-016-3439-2.

Goswami, B. B., B. Khouider, R. P. M. Krishna, P. Mukhopadhyay, and A. J. Majda, 2016: Improving synoptic and intra-seasonal variability in CFSv2 via stochastic representation of organized convection. *Geophys. Res. Lett.*, **0 (0)**, null, doi:null.

Goswami, B. B., B. Khouider, R. P. M. Krishna, P. Mukhopadhyay, and A. J. Majda, 2017: Implementation and calibration of a stochastic convective parameterization in the ncep climate forecast system. *J. Adv. Model. Earth Syst.*, submitted.

Goswami, B. B., R. P. M. Krishna, P. Mukhopadhyay, M. Khairoutdinov, and B. N. Goswami, 2015: Simulation of the Indian summer monsoon in the superparameterized Climate Forecast System version 2: Preliminary results. *J. Clim.*, **28 (22)**, 8988–9012, doi:10.1175/JCLI-D-14-00607.1.

Goswami, B. N., 2012: South Asian Monsoon. *South Asian monsoon*, W. K.-M. Lau, and D. E. Waliser, Eds., Springer Berlin Heidelberg, chap. 2, 21–72, doi:10.1007/978-3-642-13914-7_2.

Goswami, B. N., R. S. Ajayamohan, P. K. Xavier, and D. Sengupta, 2003: Clustering of synoptic activity by Indian summer monsoon intraseasonal oscillations. *Geophys. Res. Lett.*, **30 (8)**, doi:10.1029/2002GL016734.

Gottschalck, J., P. E. Roundy, C. J. S. III, A. Vintzileos, and C. Zhang, 2013: Large-scale atmospheric and oceanic conditions during the 2011-12 DYNAMO field campaign. *Mon. Weather Rev.*, **141 (12)**, 4173–4196, doi:10.1175/MWR-D-13-00022.1.

Gottwald, G. A., K. Peters, and L. Davies, 2016: A data-driven method for the stochastic parametrisation of subgrid-scale tropical convective area fraction. *Q. J. R. Meteorolog. Soc.*, **142 (694)**, 349–359, doi:10.1002/qj.2655.

Grabowski, W. W., 2001: Coupling cloud processes with the large-scale dynamics using the cloud-resolving convection parameterization (CRCP). *J. Atmos. Sci.*, **58 (9)**, 978–997, doi:10.1175/1520-0469(2001)058⟨0978:CCPWTL⟩2.0.CO;2.

Grabowski, W. W., and P. K. Smolarkiewicz, 1999: CRCP: A cloud resolving convection parameterization for modeling the tropical convecting atmosphere. *Physica D*, **133 (1)**, 171–178, doi:10.1175/1520-0469(2001)058⟨0978:CCPWTL⟩2.0.CO;2.

Guo, Y., D. E. Waliser, and X. Jiang, 2015: A systematic relationship between the representations of convectively coupled equatorial wave activity and the Madden-Julian oscillation in climate model simulations. *J. Clim.*, **28 (5)**, 1881–1904, doi:10.1175/JCLI-D-14-00485.1.

Han, Y., and B. Khouider, 2010: Convectively coupled waves in a sheared environment. *J. Atmos. Sci.*, **67 (9)**, 2913–2942, doi:10.1175/2010JAS3335.1.

Hazra, A., and V. Krishnamurthy, 2015: Space-time structure of diabatic heating in monsoon intraseasonal oscillation. *J. Clim.*, **28 (6)**, 2234–2255, doi:10.1175/JCLI-D-14-00280.1.

Hendon, H. H., and M. L. Salby, 1994: The life cycle of the Madden-Julian oscillation. *J. Atmos. Sci.*, **51**, 2225–2237, doi:10.1175/1520-0469(1994)051⟨2225:TLCOTM⟩2.0.CO;2.

Hirons, L. C., P. Inness, F. Vitart, and P. Bechtold, 2013: Understanding advances in the simulation of intraseasonal variability in the ECMWF model. Part II: The application of process-based diagnostics. *Q. J. R. Meteorol. Soc.*, **139 (675)**, 1427–1444, doi:10.1002/qj.2059.

Hohenegger, C., and B. Stevens, 2013: Preconditioning deep convection with cumulus congestus. *J. Atmos. Sci.*, **70 (2)**, 448–464, doi:10.1175/JAS-D-12-089.1.

Hung, M.-P., J.-L. Lin, W. Wang, D. Kim, T. Shinoda, and S. J. Weaver, 2013: MJO and convectively coupled equatorial waves simulated by CMIP5 climate models. *J. Clim.*, **26 (17)**, 6185–6214, doi:10.1175/JCLI-D-12-00541.1.

Jiang, X., T. Li, and B. Wang, 2004: Structures and mechanisms of the northward propagating boreal summer intraseasonal oscillation. *J. Clim.*, **17 (5)**, 1022–1039, doi:10.1175/1520-0442(2004)017⟨1022:SAMOTN⟩2.0.CO;2.

Jiang, X., and Coauthors, 2011: Vertical diabatic heating structure of the MJO: Intercomparison between recent reanalyses and TRMM estimates. *Mon. Weather Rev.*, **139 (10)**, 3208–3223, doi:10.1175/2011MWR3636.1.

Jiang, X., and Coauthors, 2015: Vertical structure and physical processes of the Madden-Julian oscillation: Exploring key model physics in climate simulations. *J. Geophys. Res. Atmos.*, **120 (10)**, 4718–4748, doi:10.1002/2014JD022375.

Johnson, R., and P. E. Ciesielski, 2013: Structure and properties of Madden-Julian oscillations deduced from DYNAMO sounding arrays. *J. Atmos. Sci.*, **70 (10)**, 3157–3179, doi:10.1175/JAS-D-13-065.1.

Johnson, R. H., T. M. Rickenbach, S. A. Rutledge, P. E. Ciesielski, and W. H. Schubert, 1999: Trimodal characteristics of tropical convection. *J. Clim.*, **12 (8)**, 2397–2418.

Kalnay, E., and Coauthors, 1996: The NCEP/NCAR 40-Year reanalysis project. *Bull. Am. Meteorol. Soc.*, **77 (3)**, 437–471, doi:10.1175/1520-0477(1996)077⟨0437:TNYRP⟩2.0.CO;2, [Available online at http://www.esrl.noaa.gov/psd/data/gridded/data.ncep.reanalysis.html].

Khairoutdinov, M. F., and D. A. Randall, 2001: A cloud resolving model as a cloud parameterization in the NCAR Community Climate System Model: Preliminary results. *Geophys. Res. Lett.*, **28 (18)**, 3617–3620, doi:10.1029/2001GL013552.

Khouider, B., J. Biello, and A. J. Majda, 2010: A stochastic multicloud model for tropical convection. *Commun. Math. Sci.*, **8 (1)**, 187–216.

Khouider, B., Y. Han, and J. Biello, 2012: Convective momentum transport in a simple multicloud model. *J. Atmos. Sci.*, **69**, 915–933, doi:10.1175/JAS-D-11-0152.1.

Khouider, B., and A. J. Majda, 2006: A simple multicloud parameterization for convectively coupled tropical waves. Part I: Linear analysis. *J. Atmos. Sci.*, **63 (4)**, 1308–1323, doi:10.1175/JAS3677.1.

Khouider, B., and A. J. Majda, 2007: A simple multicloud parameterization for convectively coupled tropical waves. Part II: Nonlinear simulations. *J. Atmos. Sci.*, **64**, 381–400, doi:10.1175/JAS3833.1.

Khouider, B., and A. J. Majda, 2008a: Equatorial convectively coupled waves in a simple multicloud model. *J. Atmos. Sci.*, **65 (11)**, 3376–3397, doi:10.1175/2008JAS2752.1.

Khouider, B., and A. J. Majda, 2008b: Multicloud models for organized tropical convection: Enhanced congestus heating. *J. Atmos. Sci.*, **65 (3)**, 895–914, doi:10.1175/2007JAS2408.1.

Khouider, B., A. J. Majda, and M. A. Katsoulakis, 2003: Coarse-grained stochastic models for tropical convection and climate. *Proc. Natl. Acad. Sci. U.S.A.*, **100 (21)**, 11 941–6, doi:10.1073/pnas.1634951100.

Khouider, B., A. St-Cyr, A. J. Majda, and J. Tribbia, 2011: The MJO and convectively coupled waves in a coarse-resolution GCM with a simple multicloud parameterization. *J. Atmos. Sci.*, **68 (2)**, 240–264, doi:10.1175/2010JAS3443.1.

Kikuchi, K., B. Wang, and Y. Kajikawa, 2012: Bimodal representation of the tropical intraseasonal oscillation. *Clim. Dyn.*, **38 (9)**, 1989–2000, doi:10.1007/s00382-011-1159-1.

Kiladis, G. N., K. H. Straub, and P. T. Haertel, 2005: Zonal and vertical structure of the Madden-Julian oscillation. *J. Atmos. Sci.*, **62 (8)**, 2790–2809, doi:10.1175/JAS3520.1.

Kiladis, G. N., M. C. Wheeler, P. T. Haertel, K. H. Straub, and P. E. Roundy, 2009: Convectively coupled equatorial waves. *Rev. Geophys.*, **47 (2)**, doi:10.1029/2008RG000266.

Kim, D., and Coauthors, 2009: Application of MJO simulation diagnostics to climate models. *J. Clim.*, **22 (23)**, 6413–6436, doi:10.1175/2009JCLI3063.1.

Kirtman, B. P., and J. Shukla, 2000: Influence of the Indian summer monsoon on ENSO. *Q. J. R. Meteorolog. Soc.*, **126 (562)**, 213–239, doi:10.1002/qj.49712656211.

Kooperman, G. J., M. S. Pritchard, M. A. Burt, M. D. Branson, and D. A. Randall, 2016: Robust effects of cloud superparameterization on simulated daily rainfall intensity statistics across multiple versions of the Community Earth System Model. *J. Adv. Model. Earth Syst.*, **8 (1)**, 140–165, doi:10.1002/2015MS000574.

Krishnamurthy, V., and J. L. Kinter, 2003: *The Indian monsoon and its relation to global climate variability*, 186–236. Springer Berlin Heidelberg, doi:10.1007/978-3-662-05285-3_10.

Lau, K.-M., and P. Chan, 1986: Aspects of the 40-50 day oscillation during the northern summer as inferred from outgoing longwave radiation. *Mon. Weather Rev.*, **114 (7)**, 1354–1367, doi: 10.1175/1520-0493(1986)114⟨1354:AOTDOD⟩2.0.CO;2.

Lau, W. K.-M., and D. E. Waliser, 2011: *Intraseasonal variability in the atmosphere-ocean climate system*. Springer Science & Business Media.

Liebmann, B., and C. Smith, 1996: Description of a complete (Interpolated) outgoing longwave radiation dataset. *Bull. Am. Meteorol. Soc.*, **77**, 1275–1277, [Available online through ftp://ftp.cdc.noaa.gov/Datasets/interp_OLR/olr.day.mean.nc].

Lin, J.-L., M.-I. Lee, D. Kim, I.-S. Kang, and D. M. W. Frierson, 2008a: The impacts of convective parameterization and moisture triggering on AGCM-simulated convectively coupled equatorial waves. *J. Clim.*, **21 (5)**, 883–909, doi:10.1175/2007JCLI1790.1.

Lin, J.-L., K. M. Weickman, G. N. Kiladis, B. E. Mapes, S. D. Schubert, M. J. Suarez, J. T. Bacmeister, and M.-I. Lee, 2008b: Subseasonal variability associated with Asian summer monsoon simulated by 14 IPCC AR4 coupled GCMs. *J. Clim.*, **21 (18)**, 4541–4567, doi: 10.1175/2008JCLI1816.1.

Lin, J.-L., and Coauthors, 2006: Tropical intraseasonal variability in 14 IPCC AR4 climate models. Part I: Convective signals. *J. Clim.*, **19 (12)**, 2665–2690.

Lin, J. W.-B., and J. D. Neelin, 2000: Influence of a stochastic moist convective parameterization on tropical climate variability. *Geophys. Res. Lett.*, **27 (22)**, 3691–3694, doi:10.1029/2000GL011964.

Lin, J. W.-B., and J. D. Neelin, 2002: Considerations for stochastic convective parameterization. *J. Atmos. Sci.*, **59 (5)**, 959–975, doi:10.1175/1520-0469(2002)059⟨0959:CFSCP⟩2.0.CO;2.

Lin, J. W.-B., and J. D. Neelin, 2003: Toward stochastic deep convective parameterization in general circulation models. *Geophys. Res. Lett.*, **30 (4)**, doi:10.1029/2002GL016203.

Lin, X., and R. H. Johnson, 1996: Heating, moistening, and rainfall over the Western Pacific warm pool during TOGA COARE. *J. Atmos. Sci.*, **53 (22)**, 3367–3383, doi:10.1175/1520-0469(1996)053⟨3367:HMAROT⟩2.0.CO;2.

Liu, P., and Coauthors, 2009: An MJO Simulated by the NICAM at 14- and 7-km resolutions. *Mon. Weather Rev.*, **137 (10)**, 3254–3268, doi:10.1175/2009MWR2965.1.

Majda, A. J., and J. A. Biello, 2003: The nonlinear interaction of barotropic and equatorial baroclinic Rossby waves. *J. Atmos. Sci.*, **60**, 1809–1821, doi:10.1175/1520-0469(2003)060⟨1809:TNIOBA⟩2.0.CO;2.

Majda, A. J., and B. Khouider, 2002: Stochastic and mesoscopic models for tropical convection. *Proc. Natl. Acad. Sci. U.S.A.*, **99 (3)**, 1123–1128, doi:10.1073/pnas.032663199.

Majda, A. J., and S. N. Stechmann, 2009a: A simple dynamical model with features of convective momentum transport. *J. Atmos. Sci.*, **66 (2)**, 373–392, doi:10.1175/2008JAS2805.1.

Majda, A. J., and S. N. Stechmann, 2009b: The skeleton of tropical intraseasonal oscillations. *Proc. Natl. Acad. Sci. USA*, **106**, 8417–8422, doi:10.1073/pnas.0903367106.

Mapes, B., S. Tulich, J. Lin, and P. Zuidema, 2006: The mesoscale convection life cycle: Building block or prototype for large-scale tropical waves? *Dyn. Atmos. Oceans*, **42 (1-4)**, 3–29, doi:10.1016/j.dynatmoce.2006.03.003.

Matsuno, T., 1966: Quasi-geostrophic motions in the equatorial area. *J. Meteorolog. Soc. Jpn. Ser. II*, **44**, 25–41.

Moncrieff, M. W., and E. Klinker, 1997: Organized convective systems in the tropical western Pacific as a process in general circulation models: a TOGA COARE case-study. *Q. J. Roy. Met. Soc.*, **123 (540)**, 805–827, doi:10.1002/qj.49712354002.

Moncrieff, M. W., D. E. Waliser, M. J. Miller, M. A. Shapiro, G. R. Asrar, and J. Caughey, 2012: Multiscale convective organization and the YOTC virtual global field campaign. *Bull. Am. Meteorol. Soc.*, **93 (8)**, 1171–1187, doi:10.1175/BAMS-D-11-00233.1.

Nakazawa, T., 1988: Tropical super clusters within intraseasonal variations over the western Pacific. *J. Meteorolog. Soc. Jpn. Ser. II*, **66 (6)**, 823–839.

Palmer, T. N., 2001: A nonlinear dynamical perspective on model error: A proposal for non-local stochastic-dynamic parametrization in weather and climate prediction models. *Q. J. R. Meteorolog. Soc.*, **127 (572)**, 279–304, doi:10.1002/qj.49712757202.

Pan, H., and W.-S. Wu, 1995: Implementing a mass flux convection parameterization package for the NMC medium-range forecast model. *NMC office note*, **409 (40)**, 20–233.

Pattanaik, S., S. Abhilash, S. De, A. K. Sahai, R. Phani, and B. N. Goswami, 2013: Influence of convective parameterization on the systematic errors of Climate Forecast System (CFS) model over the Indian monsoon region from an extended range forecast perspective. *Clim. Dyn.*, **41 (2)**, 341–365, doi:10.1007/s00382-013-1662-7.

Peters, K., T. Crueger, C. Jakob, and B. Mòbis, 2017: Improved MJO-simulation in ECHAM6.3 by coupling a stochastic multicloud model to the convection scheme. *J. Adv. Model. Earth Syst.*, doi:10.1002/2016MS000809.

Peters, K., C. Jakob, L. Davies, B. Khouider, and A. J. Majda, 2013: Stochastic behavior of tropical convection in observations and a multicloud model. *J. Atmos. Sci.*, **70 (11)**, 3556–3575, doi:10.1175/JAS-D-13-031.1.

Plant, R. S., and G. C. Craig, 2008: A stochastic parameterization for deep convection based on equilibrium statistics. *J. Atmos. Sci.*, **65**, 87–105, doi:doi:10.1175/2007JAS2263.1.

Randall, D., M. Khairoutdinov, A. Arakawa, and W. Grabowski, 2003: Breaking the cloud parameterization deadlock. *Bull. Am. Meteorol. Soc.*, **84 (11)**, 1547–1564, doi:10.1175/BAMS-84-11-1547.

Roundy, P., 2008: Analysis of convectively coupled Kelvin waves in the Indian Ocean MJO. *J. Atmos. Sci.*, **65**, 1342–1359, doi:10.1175/2007JAS2345.1.

Rui, H., and B. Wang, 1990: Development characteristics and dynamic structure of tropical intraseasonal convection anomalies. *J. Atmos. Sci.*, **47 (3)**, 357–379, doi:10.1175/1520-0469(1990)047⟨0357:DCADSO⟩2.0.CO;2.

Sabeerali, C. T., A. Ramu Dandi, A. Dhakate, K. Salunke, S. Mahapatra, and S. A. Rao, 2013: Simulation of boreal summer intraseasonal oscillations in the latest CMIP5 coupled GCMs. *J. Geophys. Res. Atmos.*, **118 (10)**, 4401–4420, doi:10.1002/jgrd.50403.

Saha, S., and Coauthors, 2014: The NCEP Climate Forecast System version 2. *J. Clim.*, **27 (6)**, 2185–2208, doi:10.1175/JCLI-D-12-00823.1.

Satoh, M., T. Matsuno, H. Tomita, H. Miura, T. Nasuno, and S.-i. Iga, 2008: Nonhydrostatic icosahedral atmospheric model (NICAM) for global cloud resolving simulations. *J. Comput. Phys.*, **227 (7)**, 3486–3514, doi:10.1016/j.jcp.2007.02.006.

Serra, Y. L., X. Jiang, B. Tian, J. Amador-Astua, E. D. Maloney, and G. N. Kiladis, 2014: Tropical intraseasonal modes of the atmosphere. *Annu. Rev. Environ. Resour.*, **39**, 189–215, doi:10.1146/annurev-environ-020413-134219.

Slingo, J. M., and Coauthors, 1996: Intraseasonal oscillations in 15 atmospheric general circulation models: results from an AMIP diagnostic subproject. *Clim. Dyn.*, **12 (5)**, 325–357, doi:10.1007/BF00231106.

Sobel, A., and E. Maloney, 2012: An idealized semi-empirical framework for modeling the Madden-Julian oscillation. *J. Atmos. Sci.*, **69 (5)**, 1691–1705, doi:10.1175/JAS-D-11-0118.1.

Sperber, K., 2004: Madden-Julian variability in NCAR CAM2.0 and CCSM2.0. *Clim. Dyn.*, **23 (3-4)**, 259–278, doi:10.1007/s00382-004-0447-4.

Sperber, K. R., H. Annamalai, I.-S. Kang, A. Kitoh, A. Moise, A. Turner, B. Wang, and T. Zhou, 2013: The Asian summer monsoon: an intercomparison of CMIP5 vs. CMIP3 simulations of the late 20th century. *Clim. Dyn.*, **41 (9)**, 2711–2744, doi:10.1007/s00382-012-1607-6.

Sperber, K. R., J. M. Slingo, P. M. Inness, and W.-M. Lau, 1997: On the maintenance and initiation of the intraseasonal oscillation in the NCEP/NCAR reanalysis and in the GLA and UKMO AMIP simulations. *Clim. Dyn.*, **13 (11)**, 769–795, doi:10.1007/s003820050197.

Stachnik, J. P., D. E. Waliser, A. J. Majda, S. N. Stechmann, and S. Thual, 2015: Evaluating MJO event initiation and decay in the skeleton model using an RMM-like index. *J. Geophys. Res. Atmos.*, **120 (22)**), doi:10.1002/2015JD023916.

Straub, K. H., P. T. Haertel, and G. N. Kiladis, 2010: An analysis of convectively coupled Kelvin waves in 20 WCRP CMIP3 global coupled climate models. *J. Clim.*, **23 (11)**, 3031–3056, doi:10.1175/2009JCLI3422.1.

Takayabu, Y. N., 1994: Large-scale cloud disturbances associated with equatorial waves. Part II: Westward-propagating inertio-gravity waves. *J. Meteorolog. Soc. Jpn. Ser. II*, **72 (3)**, 451–465.

Teixeira, J., and C. A. Reynolds, 2008: Stochastic nature of physical parameterizations in ensemble prediction: A stochastic convection approach. *Mon. Weather Rev.*, **136 (2)**, 483–496, doi:10.1175/2007MWR1870.1.

Thual, S., and A. J. Majda, 2015: A suite of skeleton models for the MJO with refined vertical structure. *Math. Clim. Weather Forecasting*, **1**, doi:10.1515/mcwf-2015-0004.

Toma, V. E., and P. J. Webster, 2010a: Oscillations of the intertropical convergence zone and the genesis of easterly waves. Part I: diagnostics and theory. *Clim. Dyn.*, **34 (4)**, 587–604, doi:10.1007/s00382-009-0584-x.

Toma, V. E., and P. J. Webster, 2010b: Oscillations of the intertropical convergence zone and the genesis of easterly waves. Part II: numerical verification. *Clim. Dyn.*, **34 (4)**, 587–604, doi: 10.1007/s00382-009-0585-9.

Waite, M., and B. Khouider, 2010: The deepening of tropical convection by congestus preconditioning. *J. Atmos. Sci.*, **67 (8)**, 2601–2615, doi:10.1175/2010JAS3357.1.

Waliser, D., and Coauthors, 2003: AGCM simulations of intraseasonal variability associated with the Asian summer monsoon. *Clim. Dyn.*, **21 (5-6)**, 423–446.

Waliser, D., and Coauthors, 2009: MJO simulation diagnostics. *J. Clim.*, **22 (11)**, 3006–3030, doi:10.1175/2008JCLI2731.1.

Wang, B., and F. Liu, 2011: A model for scale interaction in the Madden-Julian oscillation. *J. Atmos.Sci.*, **68 (11)**, 2524–2536, doi:10.1175/2011JAS3660.1.

Wang, Y., G. J. Zhang, and G. C. Craig, 2016a: Stochastic convective parameterization improving the simulation of tropical precipitation variability in the ncar cam5. *Geophys. Res. Lett.*, **43 (12)**, 6612–6619, doi:10.1002/2016GL069818.

Wang, Y., G. J. Zhang, and G. C. Craig, 2016b: Stochastic convective parameterization improving the simulation of tropical precipitation variability in the NCAR CAM5. *Geophys. Res. Lett.*, **43 (12)**, 6612–6619, doi:10.1002/2016GL069818.

Wheeler, M., and G. N. Kiladis, 1999: Convectively coupled equatorial waves: Analysis of clouds and temperature in the wavenumber-frequency domain. *J. Atmos. Sci.*, **56 (3)**, 374–399, doi: 10.1175/1520-0469(1999)056⟨0374:CCEWAO⟩2.0.CO;2.

Yashiro, H., Y. Kajikawa, Y. Miyamoto, T. Yamaura, R. Yoshida, and H. Tomita, 2016: Resolution dependence of the diurnal cycle of precipitation simulated by a global cloud-System resolving model. *SOLA*, **12**, 272–276, doi:10.2151/sola.2016-053.

Zhang, C., 2005: Madden-Julian oscillation. *Rev. Geophys.*, **43 (2)**, doi:10.1029/2004RG000158.

Zhang, C., 2013: Madden-Julian oscillation: Bridging weather and climate. *Bull. Am. Meteorol. Soc.*, **94 (12)**, 1849–1870, doi:10.1175/BAMS-D-12-00026.1.

Zhang, C., M. Dong, S. Gualdi, H. H. Hendon, E. D. Maloney, A. Marshall, K. R. Sperber, and W. Wang, 2006: Simulations of the Madden–Julian oscillation in four pairs of coupled and uncoupled global models. *Clim. Dyn.*, **27 (6)**, 573–592, doi: SimulationsoftheMadden--Julianoscillationinfourpairsofcoupledanduncoupledglobalmodels.

Zhou, L., and R. Murtugudde, 2010: Influences of Madden-Julian Oscillations on the eastern Indian Ocean and the maritime continent. *Dyn. Atmos. Oceans*, **50 (2)**, 257 – 274, doi:10.1016/j.dynatmoce.2009.12.003.

# LIST OF FIGURES

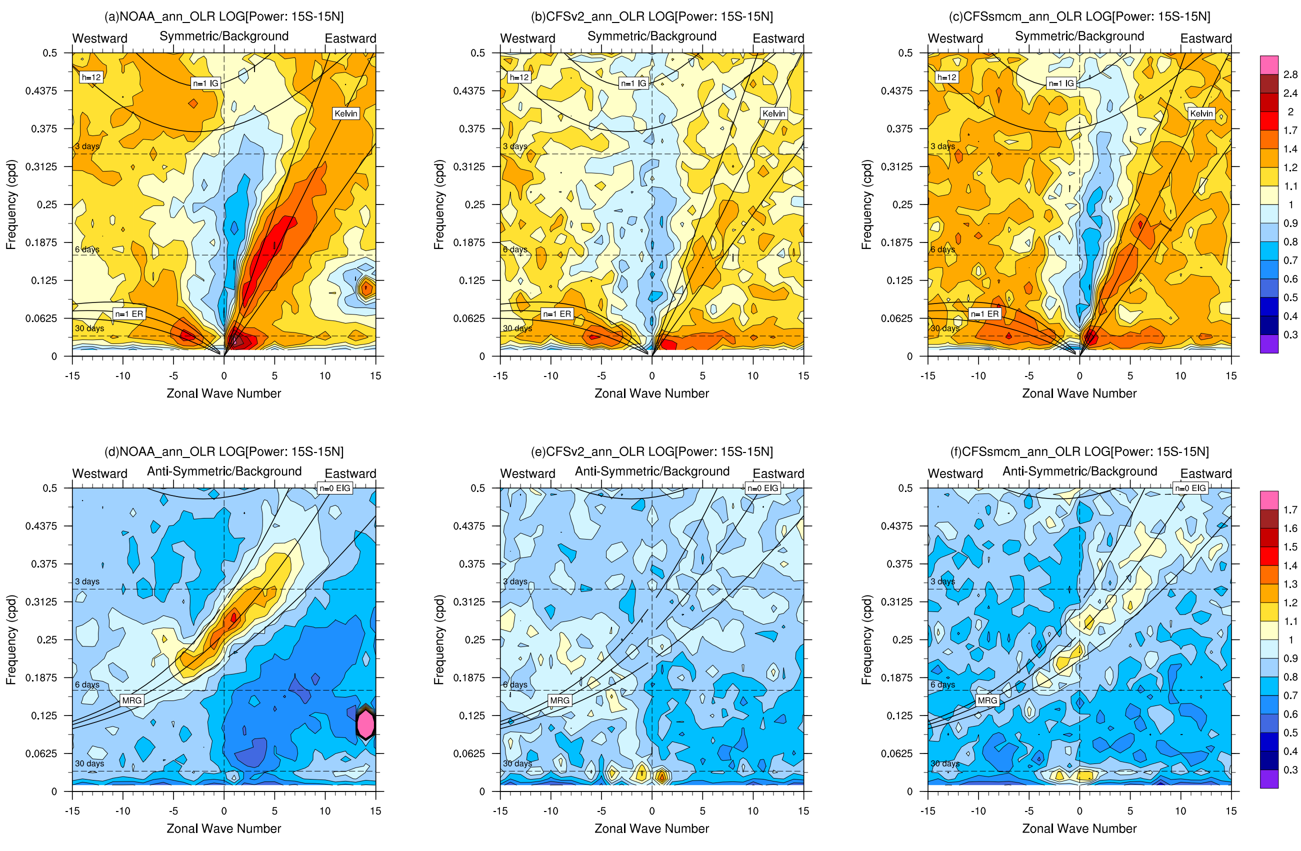


FIG. 1. Takayabu-Wheeler-Kiladis spectra of OLR from (a)NOAA, (b)CFSv2 and (c)CFSsmcm, for the symmetric component. The corresponding anti-symmetric spectra are shown in panels d, e, and f, respectively.

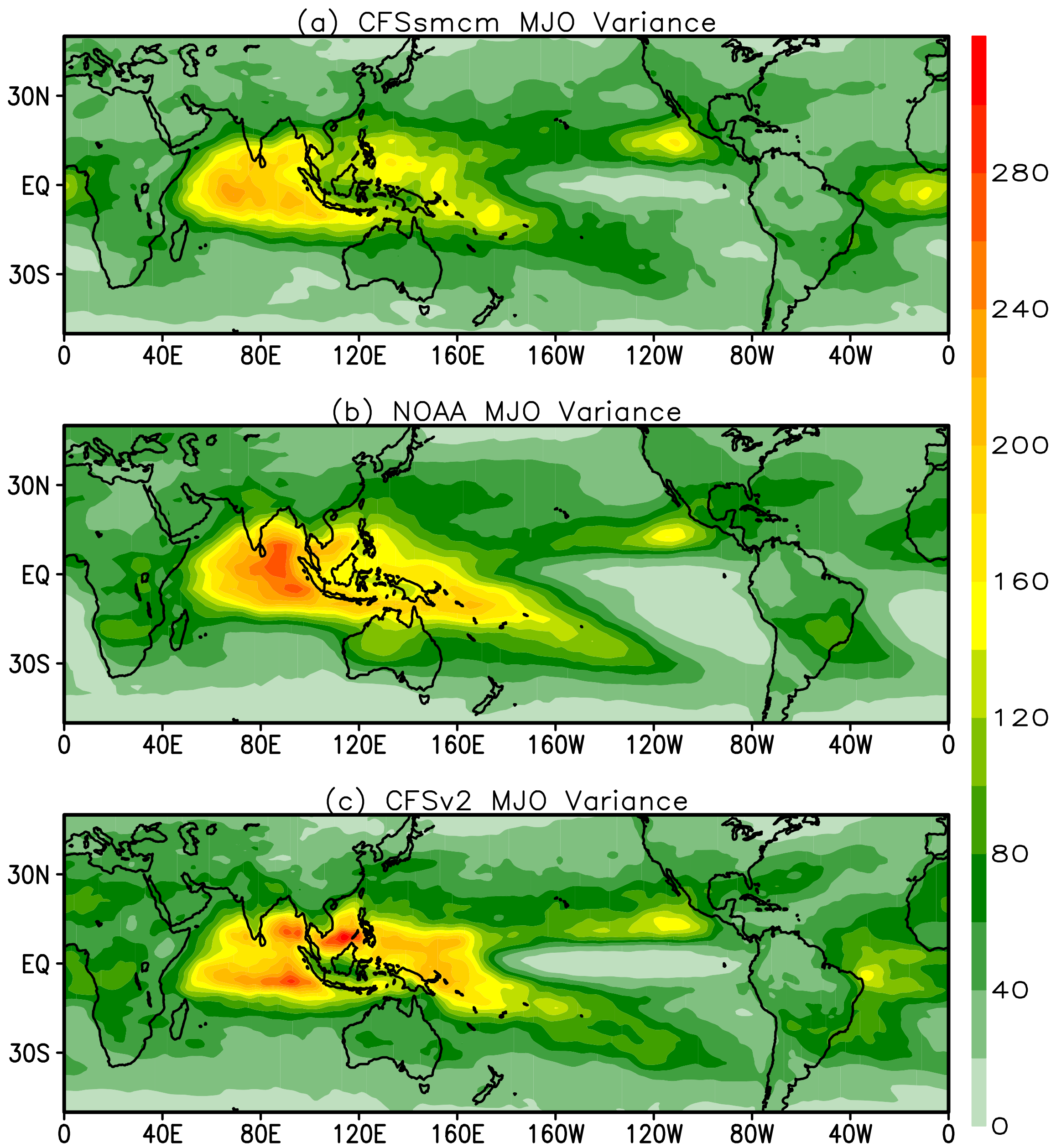


FIG. 2. Daily variance of the MJO filtered (wavenumber 1-9 and 36-90 days) OLR ($(W\ m^{-2})^2$) anomalies: (a) CFSsmcm, (b) OBS (NOAA OLR) and (c) CFSv2.

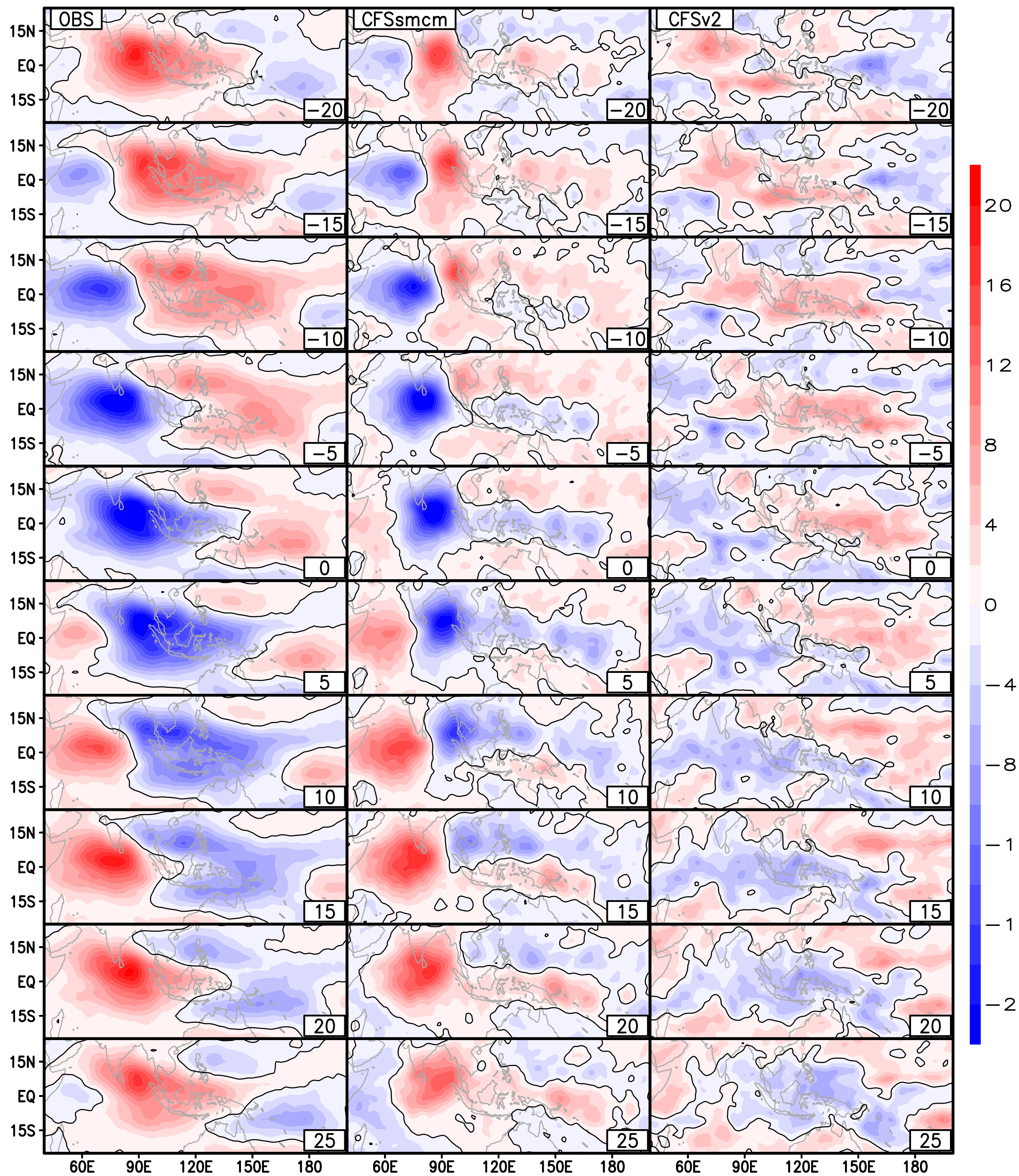


1091 FIG. 3. MJO Phase propagation. Composite of different phases of the MJO filtered OLR (W m$^{-2}$) anomalies
1092 constructed based on an MJO index averaged over 82.5°E-90°E and Eq-8.5°N. Observations are shown in the
1093 left hand side column, CFSsmcm in the middle and CFSv2 in the right hand side. Phase-lag stamps are seen in
1094 the right hand bottom corner.

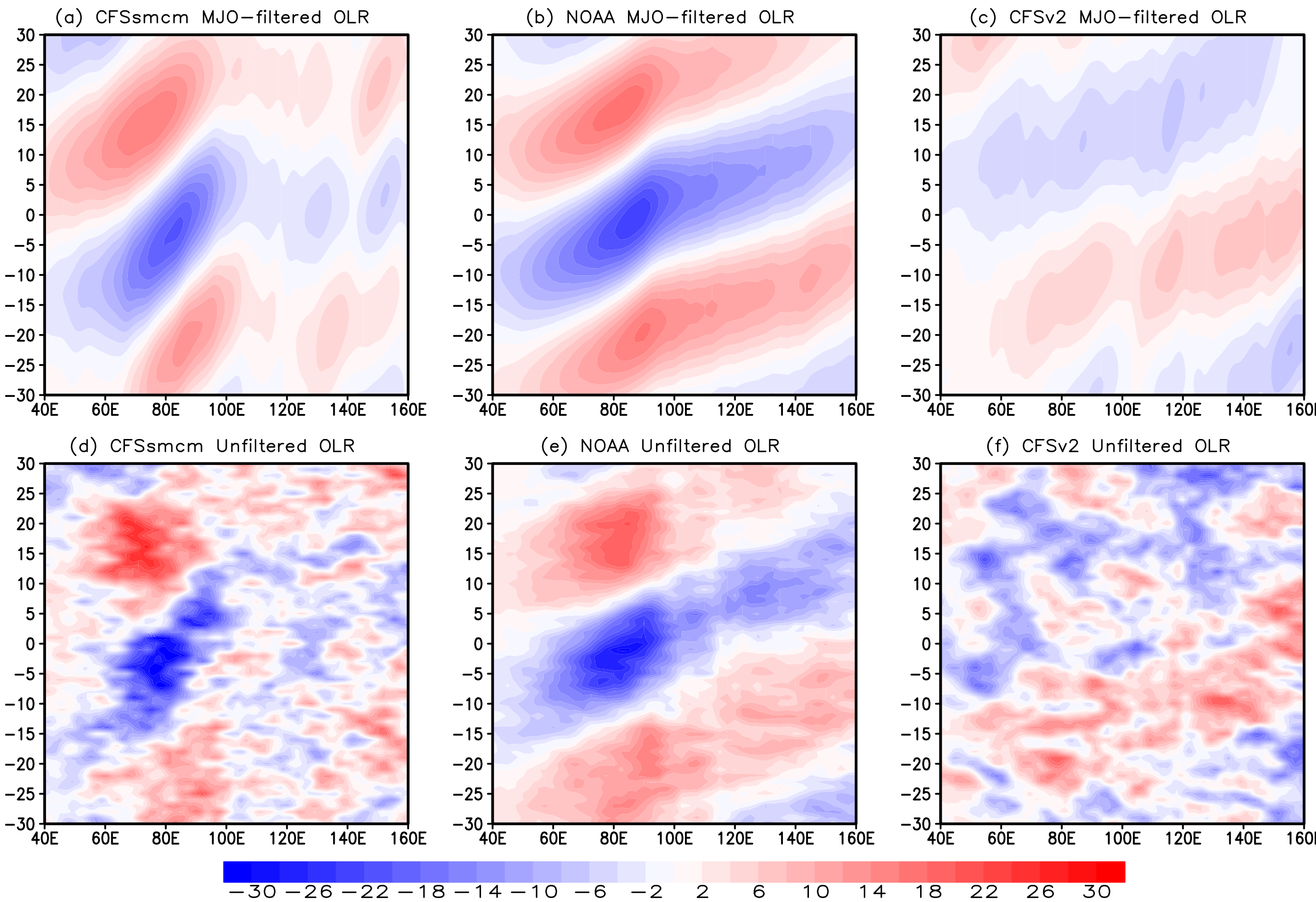


1095 FIG. 4. Hovmöller (averaged from 5°S - 5°N) plots showing MJO propagation for the MJO filtered (top three
1096 panels) and unfiltered (bottom three panels) OLR (W $m^{-2}$) anomalies.

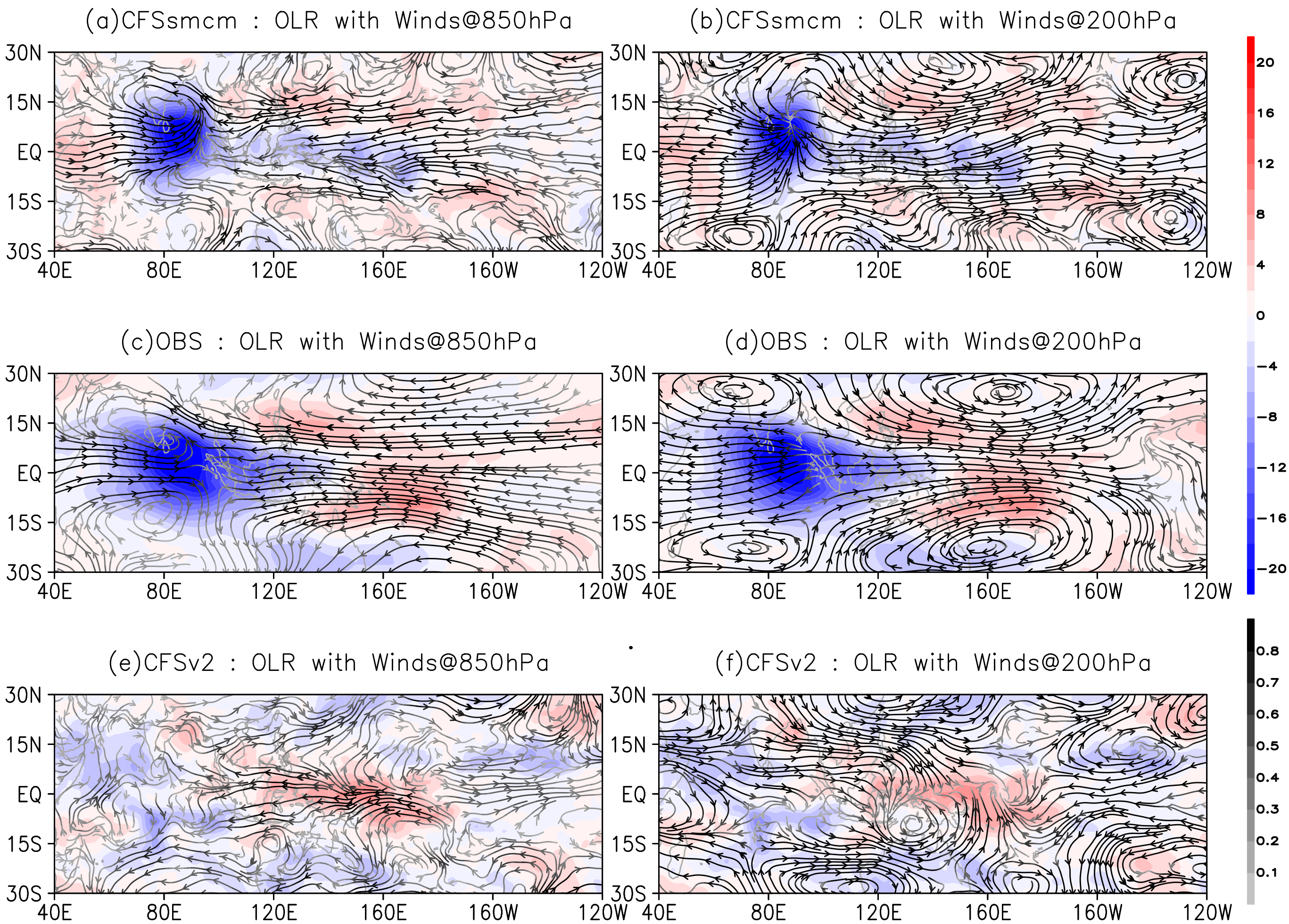


FIG. 5. MJO composite of the MJO filtered OLR (W $m^{-2}$) anomalies (in blue-white-red shading) and MJO filtered anomalous circulation (m $s^{-1}$) pattern (grey-scaled streamlines) for zero lag. The winds at 850hPa level are shown in the left hand side column panels and the same at 200hPa level are shown in the right hand side column panels.

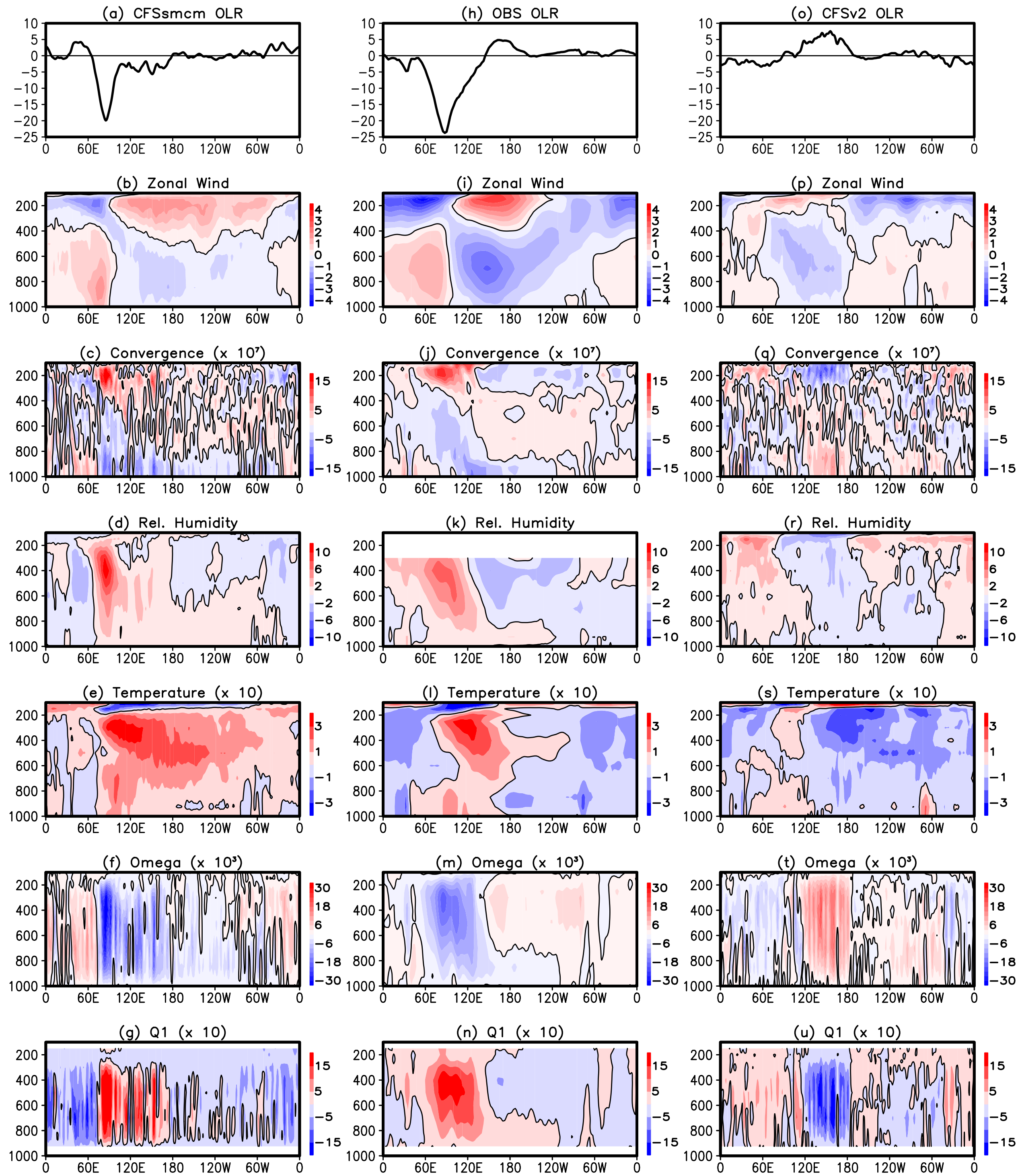


FIG. 6. Longitude-height cross section (averaged for 5°S - 5°N) of MJO composite of the MJO filtered OLR (W m$^{-2}$) anomalies and the corresponding anomalous zonal wind (m s$^{-1}$), convergence (s$^{-1}$), relative humidity (%), temperature (K), vertical velocity (Pa s$^{-1}$), and diabatic heating rate (K day$^{-1}$). CFSsmcm simulation is shown in the left hand side column, observation (NOAA OLR) in the middle and CFSv2 in the right hand side.

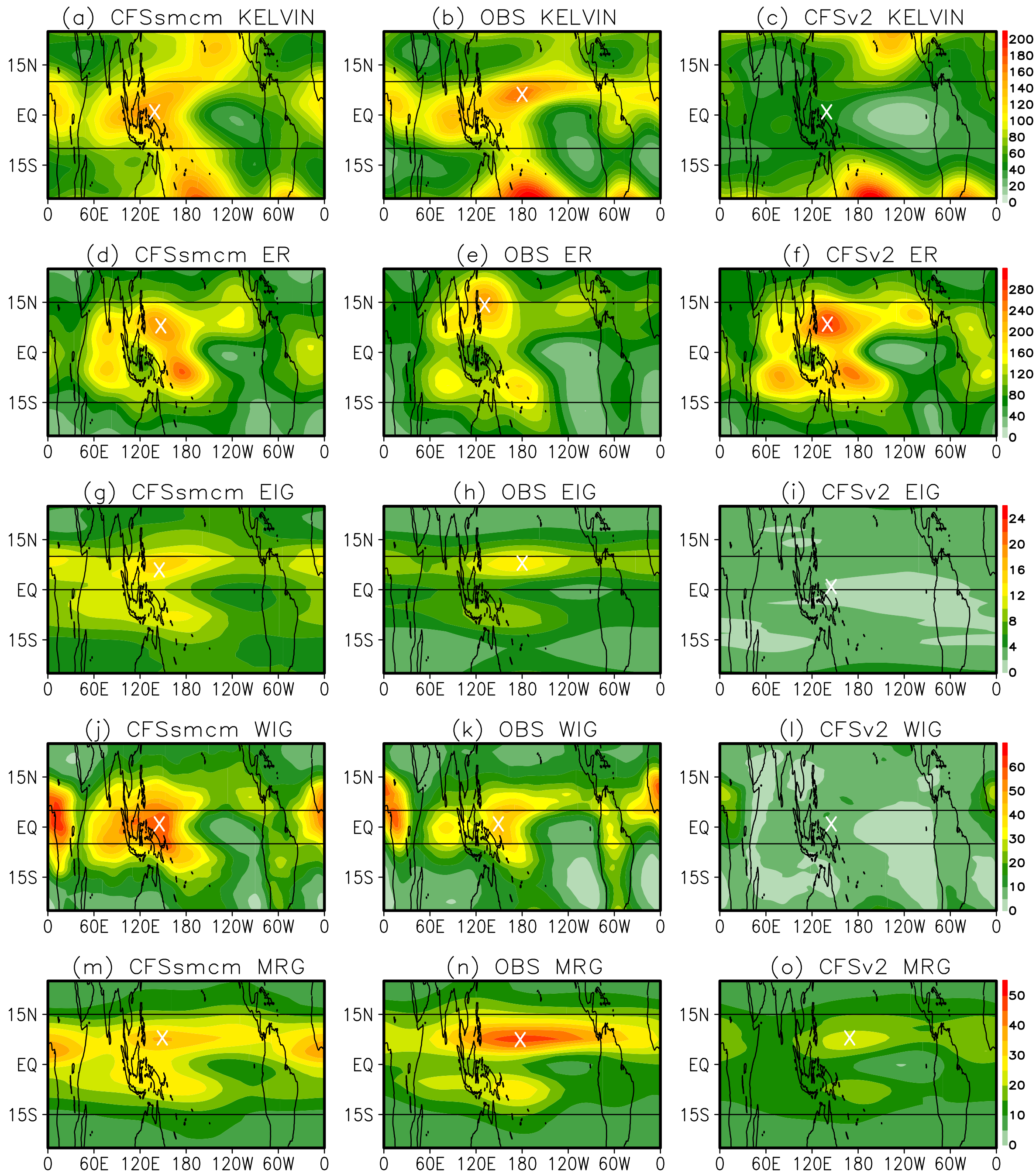


FIG. 7. Daily variance of different equatorial waves, for OLR ((W $m^{-2}$)$^2$) anomalies filtered respectively for the different waves. CFSsmcm simulation is shown in the left hand side column, observation in the middle and CFSv2 in the right hand side. The black lines in each panel, shows the zonal belt used for averaging the anomalies to plot Figure 8. The white cross-marks identify the location at which the respective indices are considered for the different equatorial waves used in the analyses towards plotting Figures 8, 9 and 10.

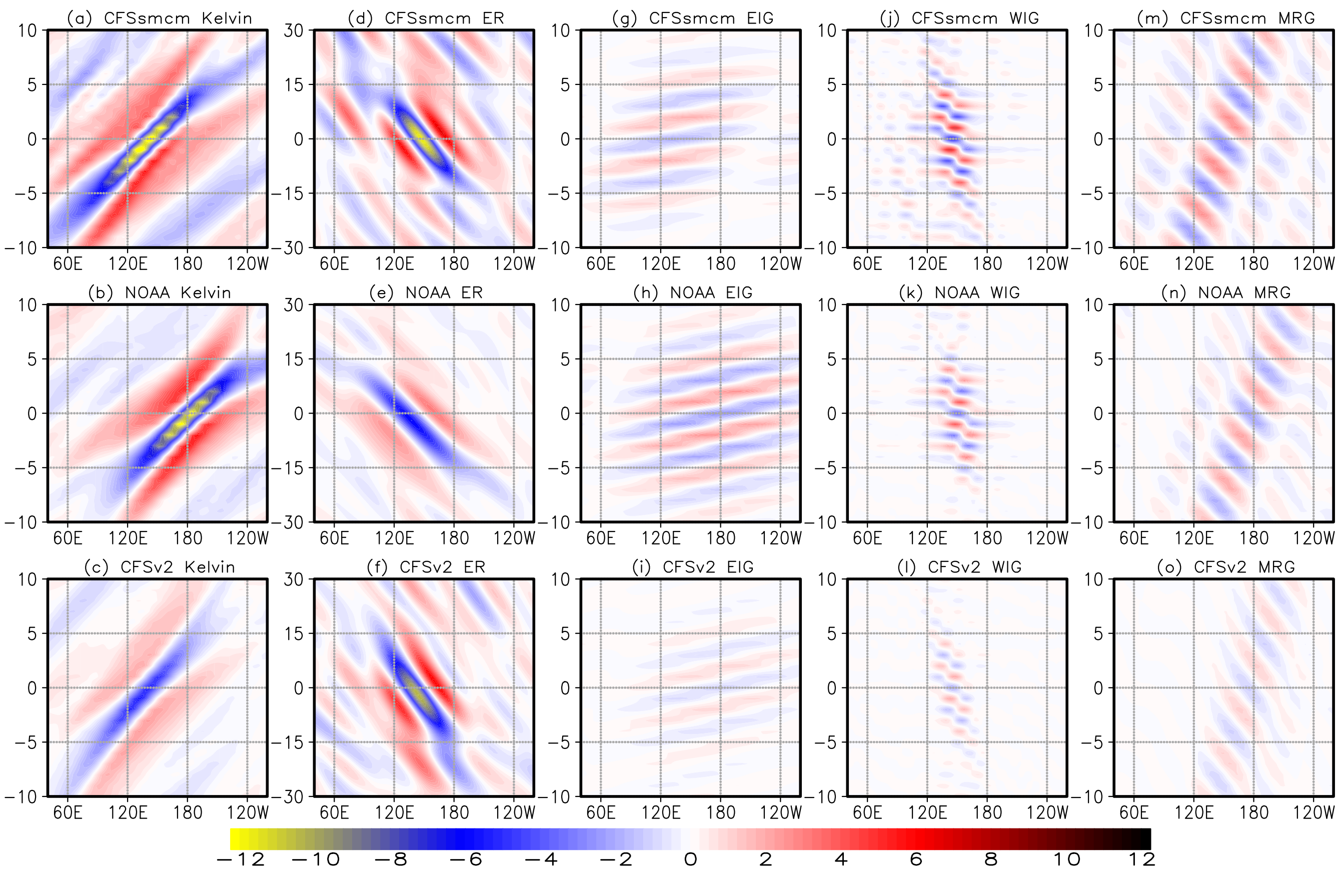


FIG. 8. Hovmöller plots (averaged over the zonal belts shown in Figure 7) showing propagation for the different equatorial waves for the respectively filtered OLR (W m$^{-2}$) anomalies. CFSsmcm simulation is shown in the top row, observation in the middle and CFSv2 in the bottom row.

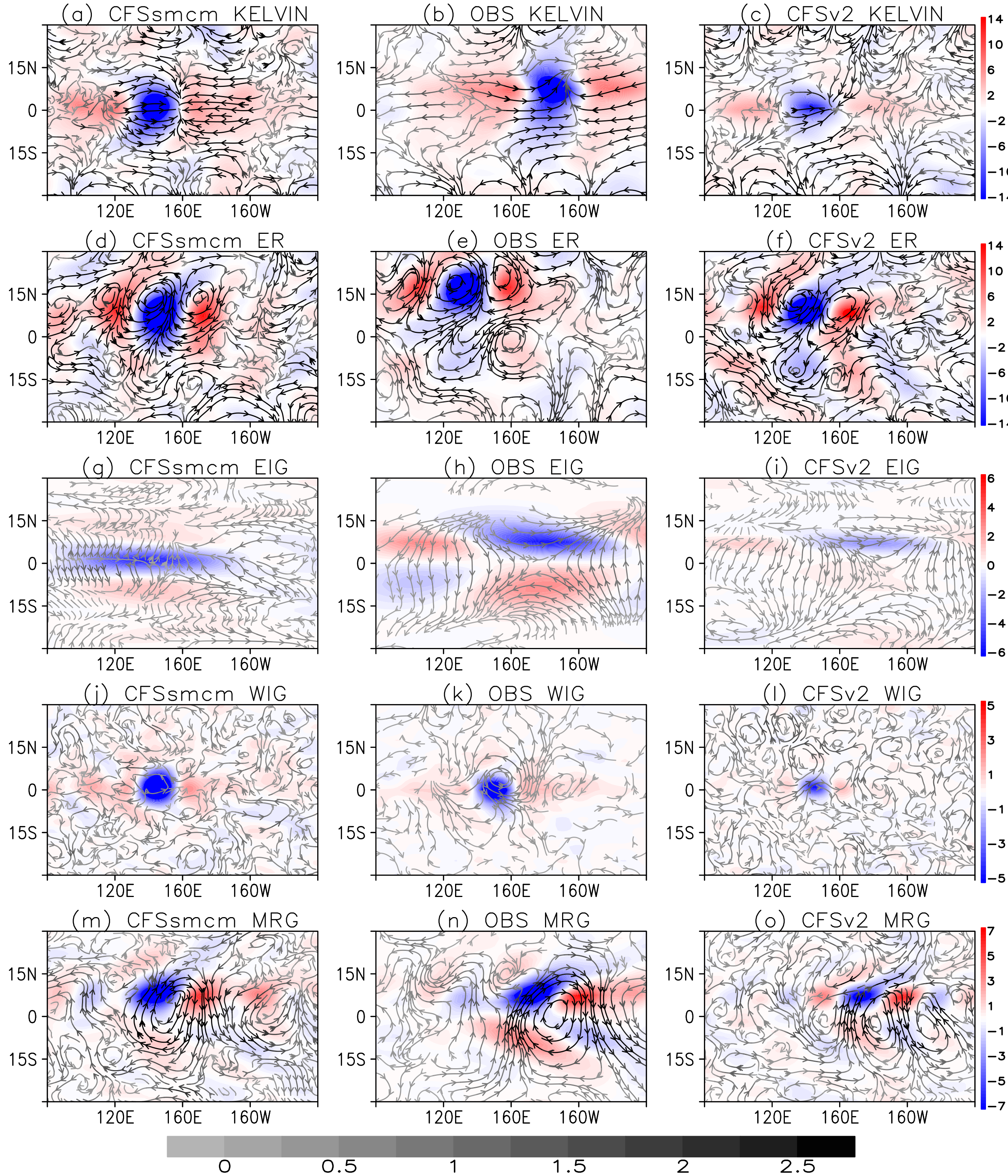


FIG. 9. Zero-lag composite of the respectively filtered OLR (W $m^{-2}$) anomalies (in blue-white-red shading) for the different equatorial waves and the corresponding anomalous 850 hPa circulation pattern (m $s^{-1}$) (grey-scaled streamlines). CFSsmcm simulation is shown in the left hand side column, observation in the middle and CFSv2 in the right hand side.

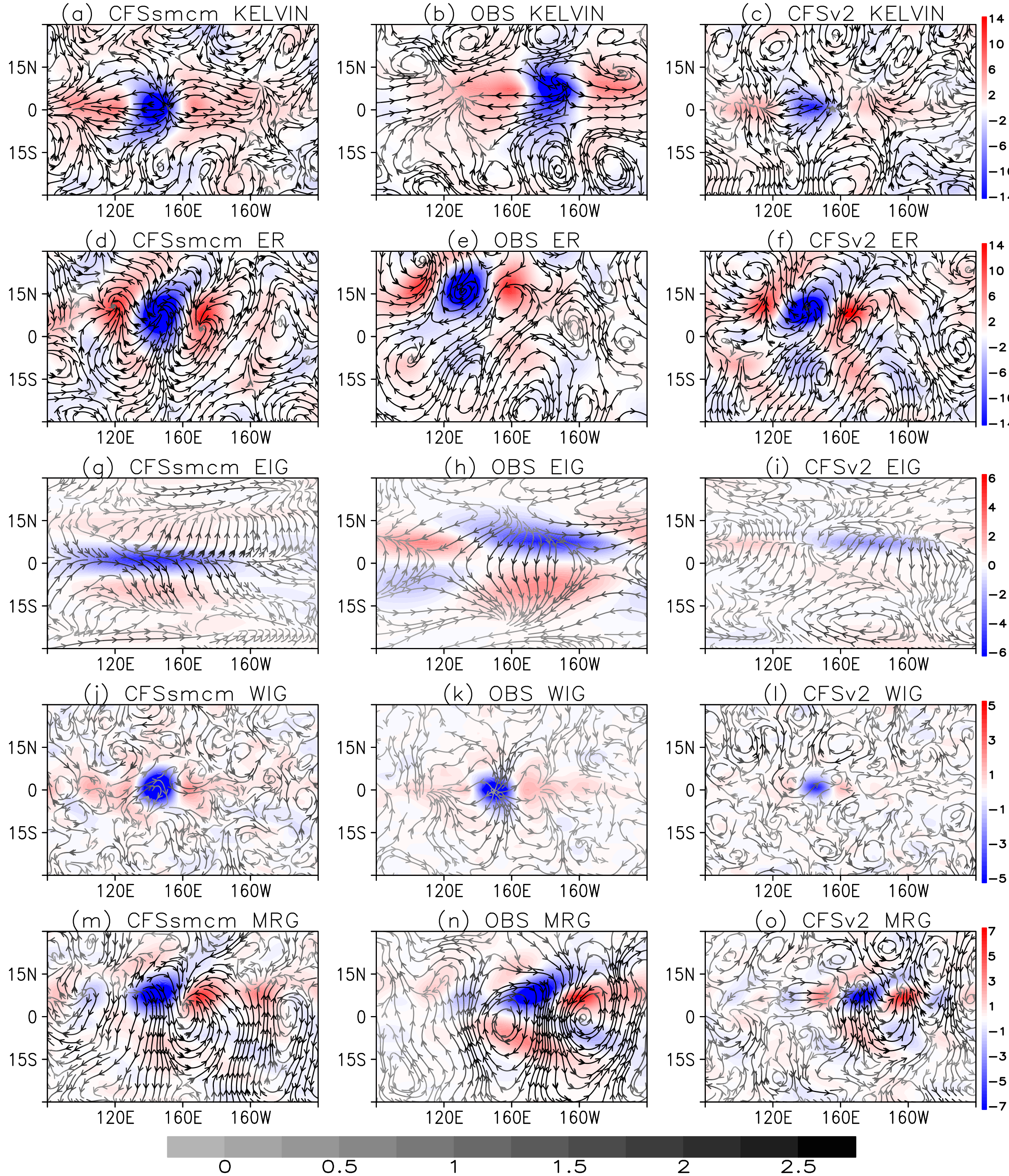


FIG. 10. Same as Figure 9, but the circulation pattern is shown for 200hPa level.

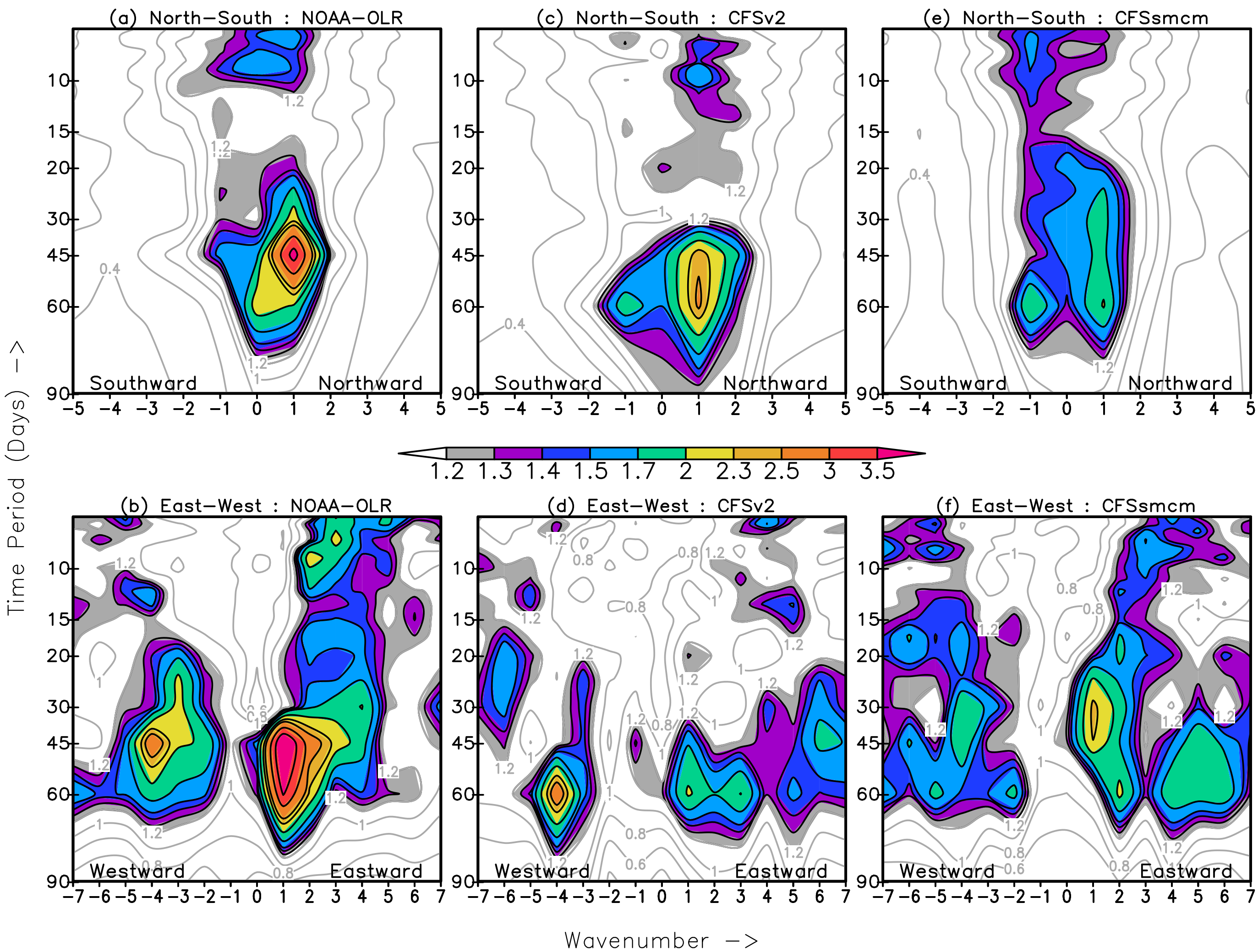


FIG. 11. Wavenumber-frequency spectra of OLR (divided by the background red spectrum) computed for the boreal summer season (JJAS). The top three panels show the north-south spectra (wavenumber 1 corresponds to the largest wave that exactly fits into 50°latitudes, from 20°S to 30°N; computed over 60°E to 100°E). The bottom three panels show the east-west spectra (wavenumber 1 corresponds to the length of the equator).

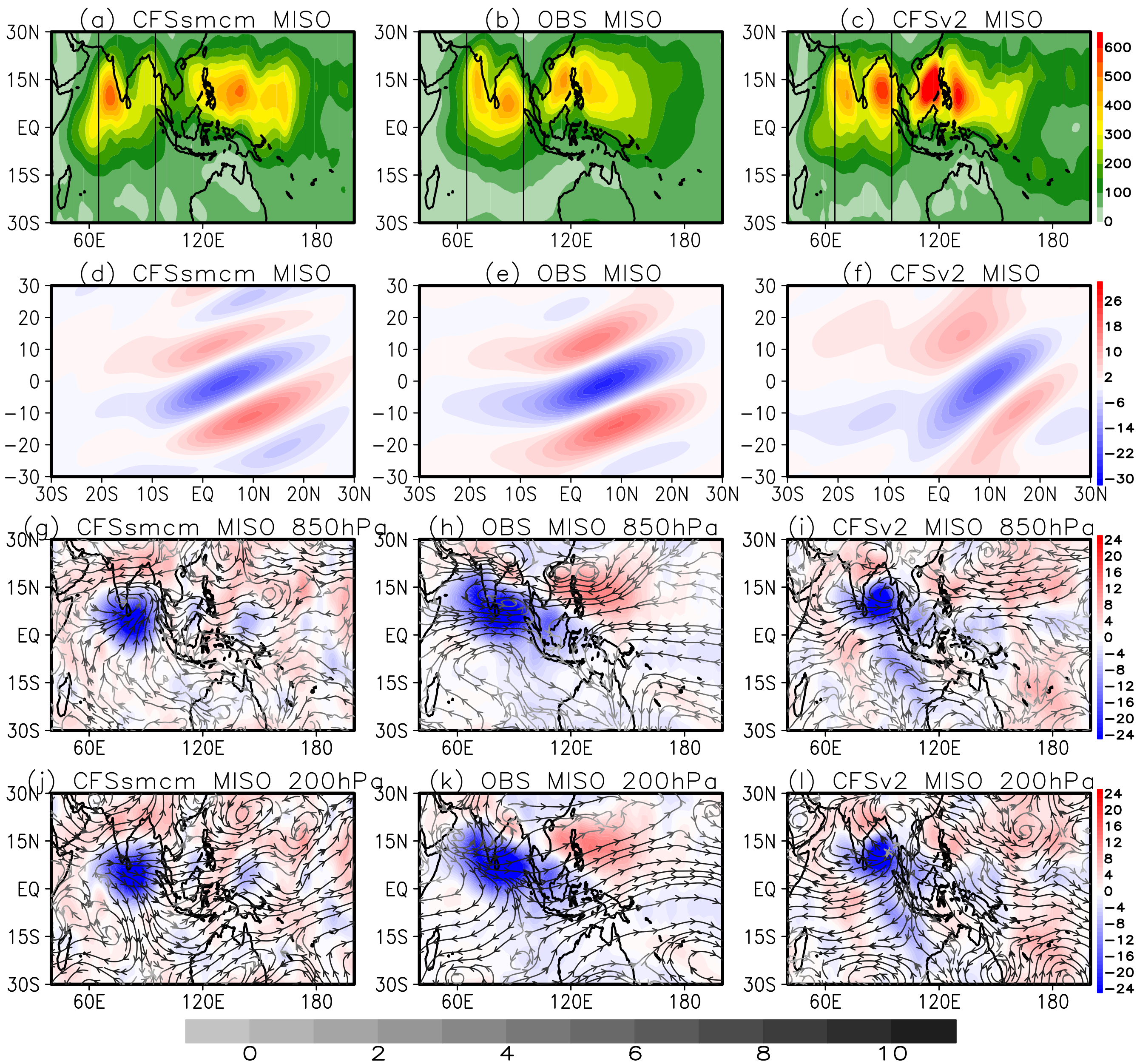


FIG. 12. Daily variance of the MISO filtered (wavenumber 0-4 and 20-90 days, in Figure 11) OLR ((W m$^{-2}$)$^2$) anomalies: (a) CFSsmcm, (b) OBS (NOAA OLR) and (c) CFSv2. Hovmöller (averaged from 65°E - 95°E, indicated by the black lines in the panels (a), (b) and (c)) plots showing MISO propagation for the MISO filtered OLR (W m$^{-2}$) anomalies: (d) CFSsmcm, (e) OBS (NOAA OLR) and (f) CFSv2. MISO composite of the MISO filtered OLR (W m$^{-2}$) anomalies (in blue-white-red shading) and MISO filtered anomalous circulation pattern (m s$^{-1}$) (grey-scaled streamlines) for zero lag. The winds at 850hPa level are shown in, (g) CFSsmcm, (h) OBS (NOAA OLR) and (i) CFSv2; and the winds at 200hPa level are shown in, (j) CFSsmcm, (k) OBS (NOAA OLR) and (l) CFSv2

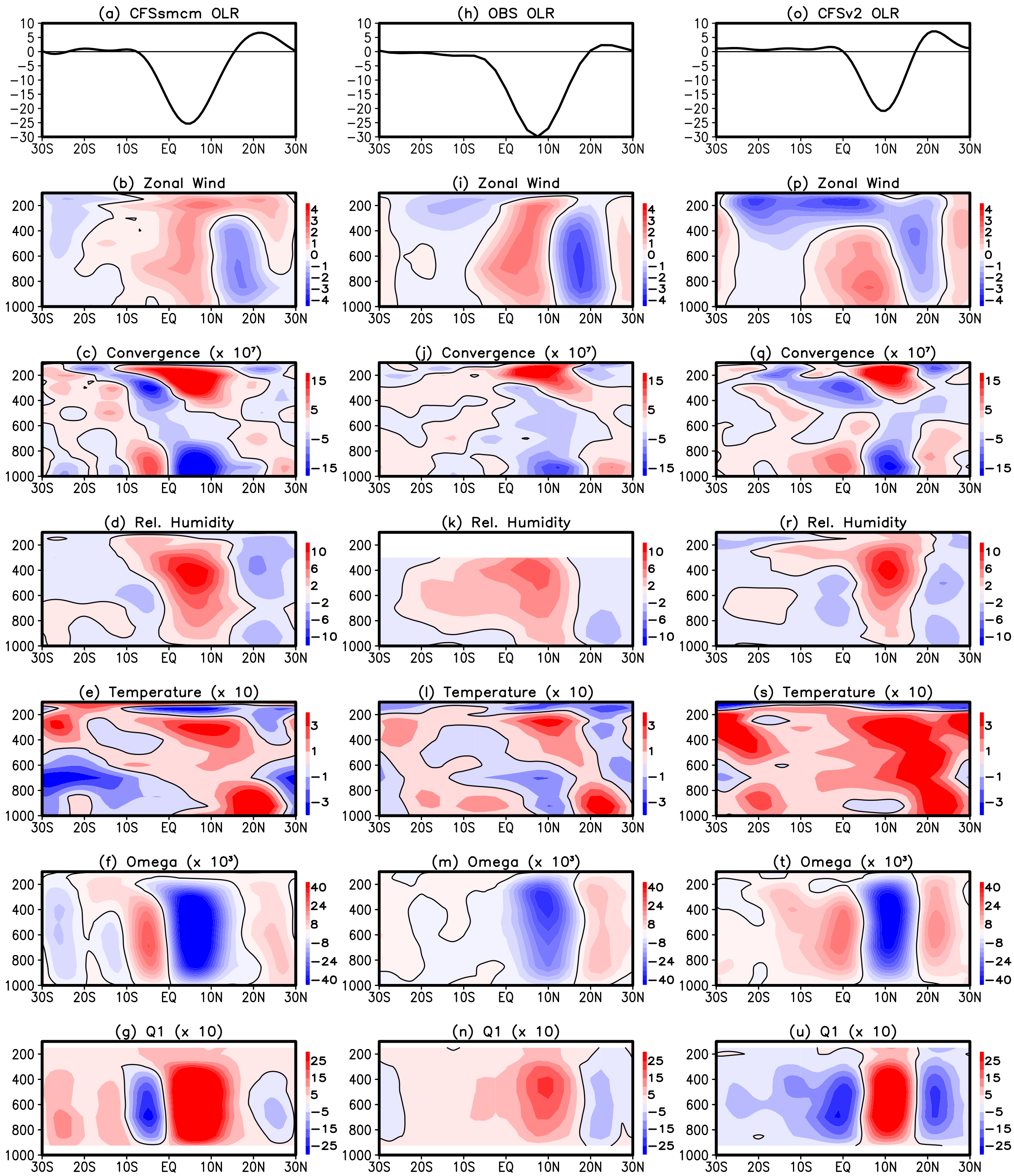


FIG. 13. Laitude-height cross section (averaged for 70°E - 90°E) of MISO composite of the MISO filtered OLR anomalies and the corresponding anomalous zonal wind ($m\ s^{-1}$), convergence ($s^{-1}$), relative humidity (%), temperature (K), vertical velocity ($Pa\ s^{-1}$), and diabatic heating rate ($K\ day^{-1}$). CFSsmcm simulation is shown in the left hand side column, observation (NOAA OLR) in the middle and CFSv2 in the right hand side.

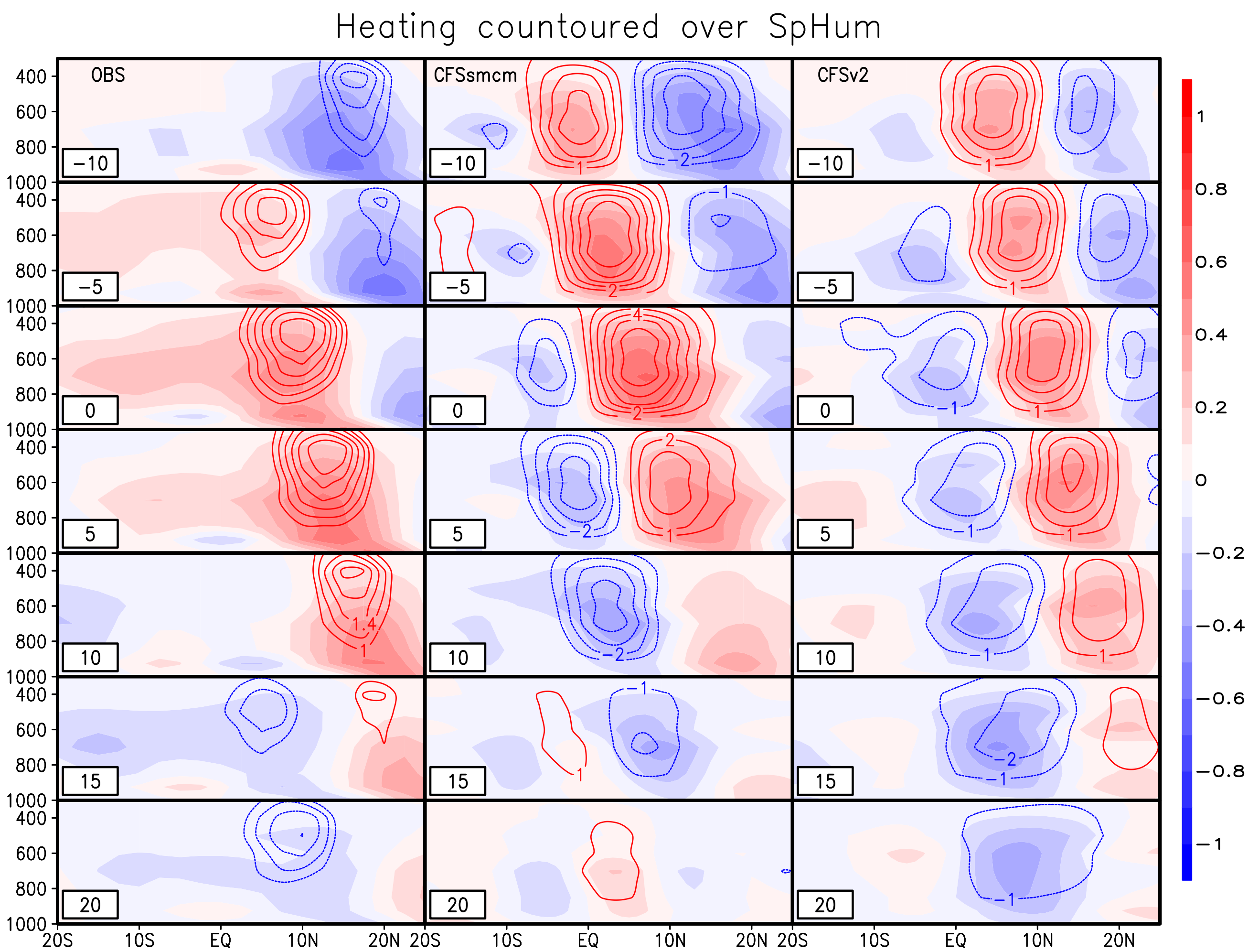


FIG. 14. MISO phase composite of latitude-height cross section (averaged for 70°E - 90°E) of the MISO filtered diabatic heating rate(K day$^{-1}$) (contours) superimposed on the corresponding Specific Humidity (g kg$^{-1}$) (in shading). Observations are shown in the left hand side column, CFSsmcm in the middle and CFSv2 in the right hand side. Phase-lag stamps are seen in the right hand bottom corner. Note: diabatic heating rate contour intervals for the observations is 0.2 K day$^{-1}$, while the same for the CFSsmcm and CFSv2 simulations is 2 K day$^{-1}$.

.